Chapter 3

Geometric and kinetic H/D isotope effects in porphycene

In this chapter we investigate the geometric and kinetic H/D isotope effects in porphycene and whether these effects shade some light upon the mechanism of the double proton transfer. First, the system will be introduced in section 3.1. Further, a review of the previous work on porphycene, related to the H/D isotope effects, will be presented in section 3.1. Secondly, the overall properties of the potential energy surface for different coordinate systems (Cartesian reaction surface and Cartesian reaction plane) will be discussed in sections 3.1 and 3.2, where the tunneling splittings for the normal as well as the deuterated porphycene will be evaluated and compared with the experimental results. Specific features of the potential energy surface around a specific minimum geometry will be shown in section 3.3, the expression of the full-dimensional anharmonic potential energy surface will be derived and it will be shown how to reduce the full dimensionality by selecting some relevant modes out of the total 3N-6 normal modes. The ground state nuclear wave functions and their relation to the geometric H/D isotope effect will be discussed in section 3.4. A comparison of the theoretically calculated geometric H/D isotope effect with the NMR experimental results will be outlined in section 3.5. In section 3.6, the kinetic isotope H/D effect as well as the effect of the barrier height and tunneling rates will be investigated.

3.1 Double hydrogen bonded system ”Porphycene”

In the following, we study the different tautomeric structures of the double hydrogen-bonded system, porphycene, shown in Fig. 3.1. Porphycene has been

synthesized by Vogel et al. [150] as a constitutional isomer of porphyrin (Fig. 3.2). Porphycene and most of its derivatives are strongly fluorescent blue pigments exhibiting remarkable photostability. Porphycene is a planar and aromatic molecule that possesses two internal hydrogen bonds involving the same donors and acceptors, i.e. nitrogen atoms. Two internal hydrogen atoms undergo an exchange between these nitrogen atoms giving rise to three different tautomeric forms, trans, cis$_a$ and cis$_b$. In the trans configuration, the two hydrogens are located on two opposite nitrogen atoms, see Fig. 3.1.

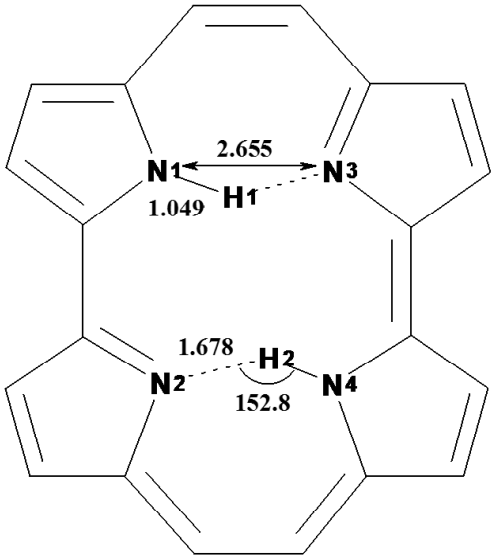

Figure 3.1: The (B3LYP/6-31+G(d,p)) optimized values of the hydrogen bond parameters inside the cavity of the trans tautomer of porphycene. Notice that the N-N distance as well as the N-H-N angle is in fair agreement with the experimental values of 2.63 Å [150] and 153° [151], respectively.

The two hydrogen atoms are located on two adjacent nitrogen atoms (for instance, N1 and N2 or N1 and N3) in the cis tautomers. The arrangement of two protons on the adjacent nitrogen atoms (N1 and N2), cis$_a$, is energetically much more favourable than that of the other possible species (where the two hydrogens are on the adjacent nitrogens N1 and N3), cis$_b$. We shall not consider the latter because of its high energy compared to the former and from now on we shall call cis$_a$ the cis tautomer.

From the theoretical point of view porphycene is an example for a system exhibiting a Hartree-Fock instability. This issue was addressed by Hohlneicher and coworkers who showed that Hartree-Fock theory predicts a ground state of

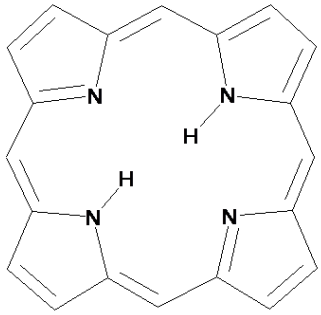

Figure 3.2: The trans tautomer of porphyrin.

low symmetry with pronounced bond length alternations. This failure can only be compensated by accounting for electron correlations, e.g., at the level of density functional theory [152].

We have investigated the stationary points along the concerted and stepwise double proton transfer pathways shown in Fig. 3.3 employing density functional theory (at different levels of theories). In order to reduce the uncertainty in the barrier heights, we further calculated the stationary points using Møller Plesset perturbation theory (MP2). For density functional theory method, we employed besides the standard B3LYP functional the MPW1K functional, which has been developed especially for the kinetics of radical hydrogen atom transfer reactions [153]. All quantum chemical calculations have been performed using Gaussian98/03 [154, 155] program packages. The molecular geometry of the stationary points of porphycene were fully optimized using the gradient minimization technique. The global minimum is characterized by having zero gradient norms and by diagonalizing the matrix of the second derivatives. Figure 3.4 reveals the optimized geometries of trans and cis tautomers of porphycene and the corresponding saddle points (transition states) calculated by DFT(B3LYP) method combined with a 6-31G(d,p) basis set as implemented in Gaussian03 program package [155]. The stationary points' energies calculated with different methods and levels of theories, are collected in Table 3.1.

All methods predict the barrier for the concerted pathway to be higher than that along the stepwise pathway ($E_{TS(trans,trans)} > E_{TS(cis,trans)}$). An interesting aspect which has been first noted by Koslowski and coworkers [156] concerns the effect of the ZPE. As can seen from Table 3.1, inclusion of the harmonic ZPE reverses the energetics of the two pathways, i.e. for the ZPE-corrected barriers, the concerted pathway is preferred. Of course, this is not surprising since there is one

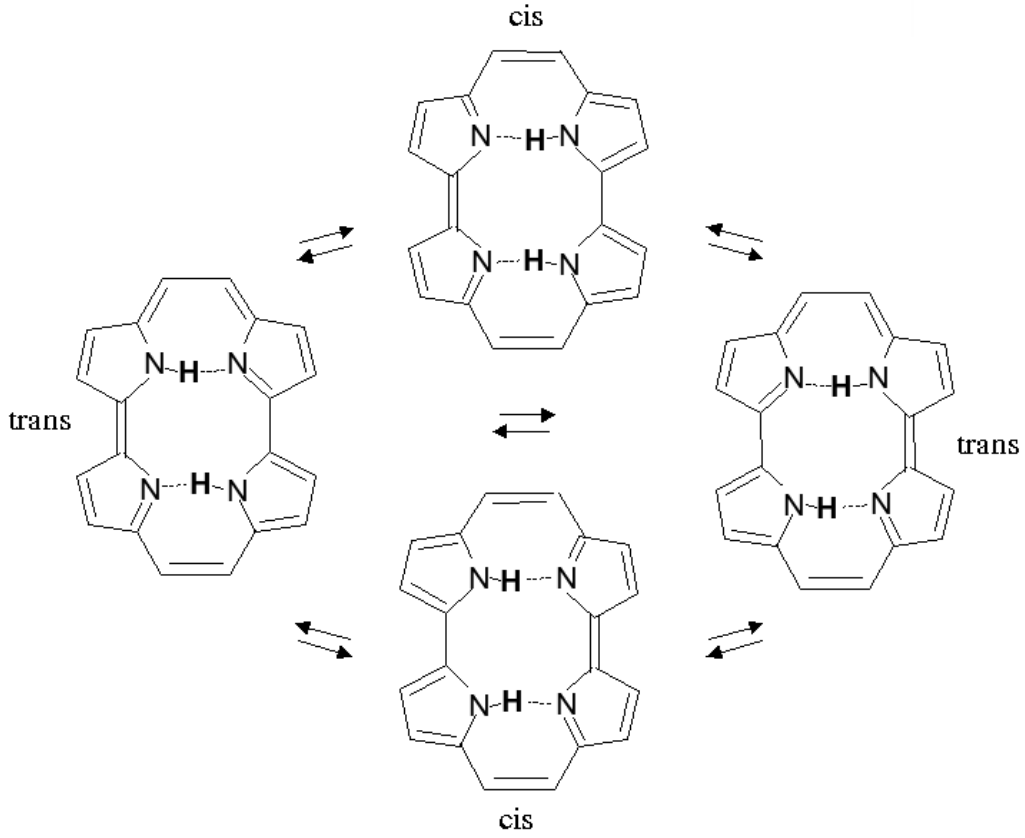

Figure 3.3: Concerted (trans-trans) versus stepwise (trans-cis-trans) double hydrogen transfer mechanisms in porphycene.

	6-31G(d,p)		6-31+G(d,p)			
	B3LYP	B3LYP/ZPE	B3LYP	B3LYP/ZPE	MPW1K	MP2
E(trans)	0.00	0.00	0.00	0.00	0.00	0.00
E(cis)	2.08	1.61	2.30	0.59	1.68	2.65
$E_{TS(cis,trans)}$	4.15	0.76	4.68	5.54	2.42	3.75
$E_{TS(trans,trans)}$	6.23	0.62	6.45	3.03	3.41	5.23

Table 3.1: Energetics (in kcal/mol) of the stationary points of porphycene for different quantum chemical methods and at different levels of theories. The B3LYP/ZPE energies include the ZPE correction.

more imaginary frequency for TS(trans,trans) than for TS(cis,trans). This conclusion is depicted in Figs. 3.5 and 3.6, where one can see in Fig. 3.5 that the cis and its transition state are energetically more preferable than the transition state

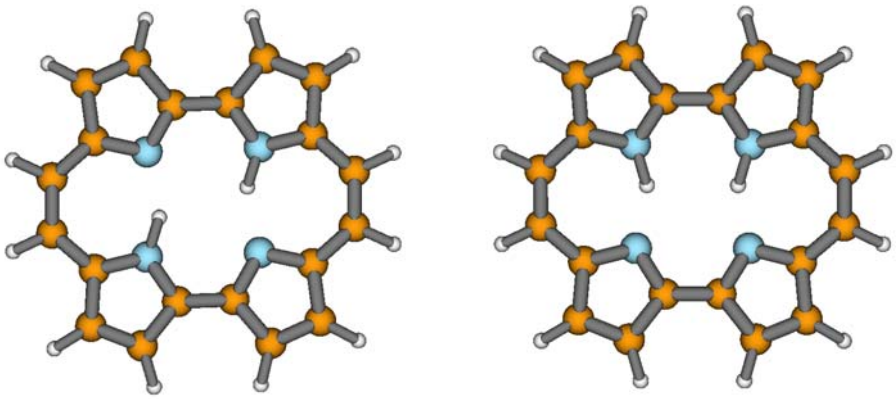

(a) (b)

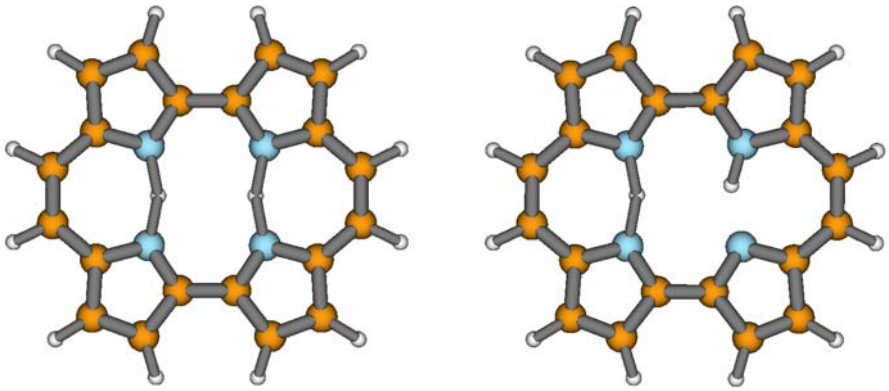

(c) (d)

Figure 3.4: The optimized stationary points of porphycene obtained from DFT/B3LYP/6-31G(d,p) calculations for (a) trans tautomer, (b) cis tautomer, (c) transition state of the trans-trans tautomerization and (d) transition state of the trans-cis tautomerization (Note: this presentation is rotated by 90° compared to Fig. 3.1).

of the trans-trans conversion, therefore, the stepwise pathway wins, while Fig. 3.6 reveals that the transition state of the trans-trans interconversion has lower energy than the cis and its transition state and hence the concerted pathway dominates. Notice that, the ambient temperature is about 0.6 kcal/mol which is approximately equal to the relative value of the energy of TS(trans,trans’), i.e. under thermal conditions the proton transfer rate will be mainly over-the-barrier (follows TST). Another conclusion can be seen in Fig. 3.6 that is the cis isomer will be energetically higher than its transition state which means that the cis isomer can be considered as a saddle point for the trans-trans tautomerization. From this one could draw the conclusion that the tautomerization reaction in porphycene might

proceed synchronously, however, this is within the harmonic approximation.

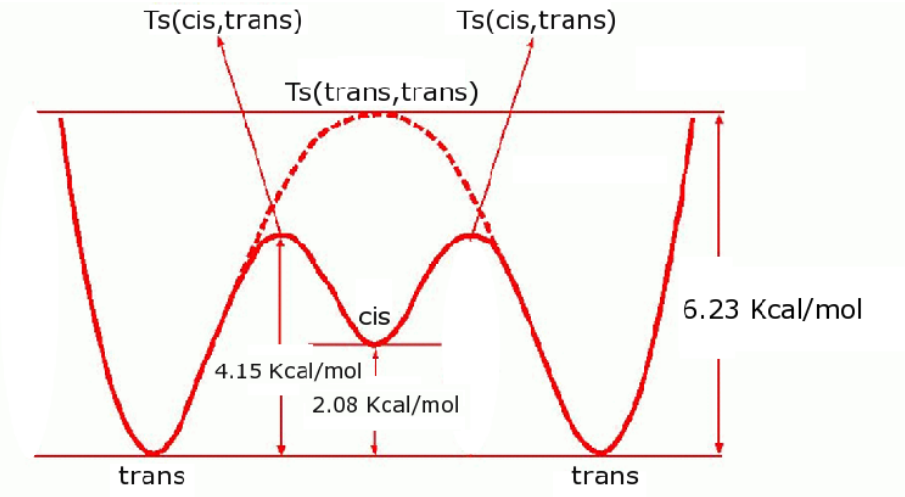

Figure 3.5: Potential energy profile representing the energetics of the stationary points without the zero point energy calculated at DFT/B3LYP/6-31G(d,p) level of calculation. In this case the tautomerization reaction prefers the stepwise mechanism.

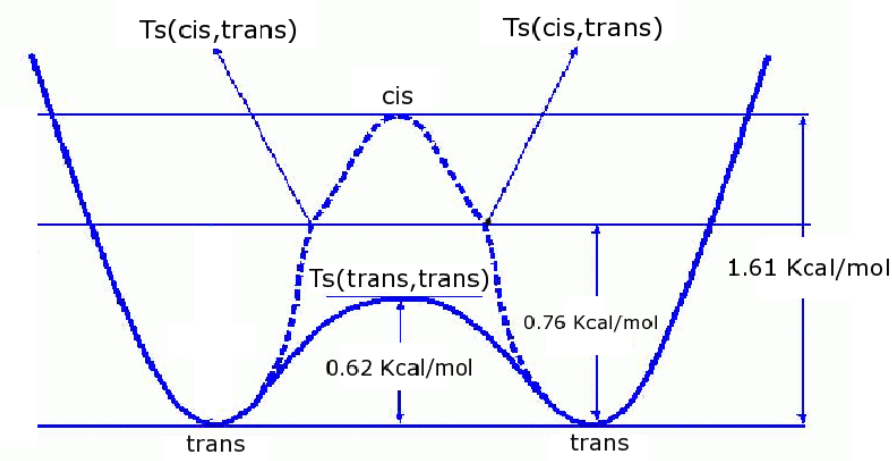

Figure 3.6: Potential energy profile representing the energetics of the stationary points with the zero point energy (harmonic approximation) calculated at DFT/B3LYP/6-31G(d,p) level of calculation. In this case the tautomerization reaction prefers the concerted mechanism.

Since porphycene is a big molecule, we will consider the moderate level of theory, i.e. 6-31G(d,p), in the calculation of the potential energy surface in which we need to calculate a large number of points. In contrast, for the calculation

of the stationary points' potential energy surface using the gradient minimization technique (geometry optimization), we will use the higher level of theory, i.e. 6-31+G(d,p).

Since we restrict our study in section 3.3 to the vicinity of the minimum of the potential energy surface (i.e. the barrier heights are considered as not so important), we will consider the normal modes as the employed coordinate system. For preparation, we briefly present results on the normal modes (corresponding to the vibrations describing the motion of the inner protons) obtained from DFT calculations mentioned above. Inspecting the normal modes of the trans tautomer (Fig. 3.4a), table 3.2, reveals that NH stretching mode is the most intense band which has no counterpart in the experimental spectra, see Ref. [157]. Malsch and Hohlneicher suggested that the absence of the NH stretching vibration is attributed to the band broadening because of a rapid motion of the proton in the hydrogen bridge and therefore completely disappears. They could not assign the stable tautomer from the infrared experimental results, so that we will present as well the normal modes of the cis tautomer, Table 3.3. Furthermore, the modes with imaginary frequencies of the transition states for the trans-trans and trans-cis interconversions are given in Table 3.4.

No.	Sym.	$\widetilde{\omega}$ (cm^{-1})	Int. (KM/Mole)	Ass.
49	B_g	934	0.00	Asym. combination of the N-H out-of-plane bending
56	A_g	1000	137.03	Sym. combination of the N-H out-of-plane bending
93	B_u	1631	32.98	Asym. combination of the N-H in-plane bending
94	A_g	1662	0.00	Sym. combination of the N-H in-plane bending
95	A_g	2891	5.45	Sym. combination of the N-H stretching
96	B_u	2892	434.94	Asym. combination of the N-H stretching

Table 3.2: The normal modes for the trans tautomer (Fig. 3.4) (associated with the inner protons' motion), the corresponding non-scaled wave numbers (in cm^{-1}) and assignments. The molecular symmetry is C_{2h}. DFT/B3LYP/6-31G(d,p) level of theory was used as implemented in Gaussian03 [155].

From this normal mode analysis, the transition state of the trans-trans intercon-

No.	Sym.	$\widetilde{\omega}$ (cm^{-1})	Int. (KM/Mole)	Ass.
53	A_2	976	0.00	Asym. combination of the N-H out-of-plane bending
58	B_1	1051	128.20	Sym. combination of the N-H out-of-plane bending
88	B_2	1561	41.72	Asym. combination of the N-H in-plane bending
94	A_1	1673	27.69	Sym. combination of the N-H in-plane bending
95	B_2	2602	5.47	Asym. combination of the N-H stretching
96	A_1	2640	522.54	Sym. combination of the N-H stretching

Table 3.3: The normal modes for the cis tautomer (Fig. 3.4) (associated with the inner protons' motion), the corresponding non-scaled wave numbers (in cm^{-1}) and assignments. The molecular symmetry is C_{2v}. DFT/B3LYP/6-31G(d,p) level of theory was used as implemented in Gaussian03 [155].

Second order saddle point (trans-trans)			
No.	Sym.	$\widetilde{\omega}$ (cm^{-1})	Ass.
01	B_{3g}	-1205	Sym. combination of the N-H stretching
02	B_{2u}	-1067	Asym. combination of the N-H stretching
Transition state (trans-cis)			
01	A'	-1213	N-H stretching of the moving proton

Table 3.4: The normal modes (with imaginary frequencies) for the second order saddle point (Fig. 3.4) of trans-trans tautomerization as well as the transition state (Fig. 3.4) of the trans-cis interconversion (associated with the inner protons' motion) and assignments. The molecular symmetries are D_{2h} and C_s for the saddle point and transition state, respectively. DFT/B3LYP/6-31G(d,p) level of theory was used as implemented in Gaussian03 [155].

version is a second order saddle point because it has two imaginary frequencies (stretching vibrations), therefore, one can conclude that the reaction coordinate at the transition state of the trans-trans tautomerization is definitely dominated by the stretching vibration (specifically the symmetric one).

Using density functional theory calculations, Wu and coworker predicts that

porphycene as a free base is more stable than porphyrin [158]. This stability is due to the rectangular shape of the cavity hosting the hydrogen bonds which leads to a linear arrangement of N-H$\cdots$N and a smaller N-N distance (2.63Å in porphycene [150] compared to 2.90Å in porphyrin [159]). In metal complexes the relative stabilities of the porphyrin and porphycene are reversed since the larger cavity in porphyrin facilitate the metal accommodation inside the cavity. The tighter cavity in porphycene enhances the strength of the hydrogen bonds as compared to that of porphyrin. The N-N distance value predicted by X-ray (2.63 Å) [150] lies between those calculated for trans (2.65 Å) and cis (2.61 Å) forms [158] suggesting the presence of both species in the crystal. Therefore, this kind of traditional hydrogen bond has medium strength, which is characterized by localized ground state wave function.

Although the Infrared spectrum could not give clear evidence for the most stable isomer [157], quantum chemical calculations performed by Kozlowski et al. [156] who, by using DFT(B3LYP), showed that the trans form (Fig. 3.1) is about 2.4 kcal/mol more stable than the cis one (in the present calculations, it is 2.3 kcal/mol in case of B3LYP/6-31+G(d,p)). Localization and transfer of the N-protons in porphyrin and porphycene have been investigated using variable-temperature high-resolution ^{15}N NMR spectroscopy [160] (for a review, see also Ref. [161]). At elevated temperatures, the spectra of porphyrin as well as porphycene reveal one signal, i.e. at high temperatures a very fast proton transfer apparently takes place, see Fig. 3.7. Lowering the temperature from 356 to 192 K leads to a line broadening in case of porphyrin, i.e. the process becomes frozen until complete separation of the =N- and NH signals. On the other hand, porphycene does not show line-broadening as the temperature is lowered, i.e. no ”freezing” of the protons’ motions, but a splitting into four sharp peaks, assigned to two non-equivalent asymmetric hydrogen transfer systems. The tautomerization in each of them is extremely rapid even at very low temperature. Two possibilities were proposed that are: a) two non-equivalent porphycene molecules in the crystal, each contains two proton transfer systems, this case involves trans-trans equilibria; b) four different tautomeric forms are involved in the crystal, this indicates a presence of trans and cis tautomeric forms. From these measurements, one cannot decide whether the tautomerization mechanism is concerted or stepwise.

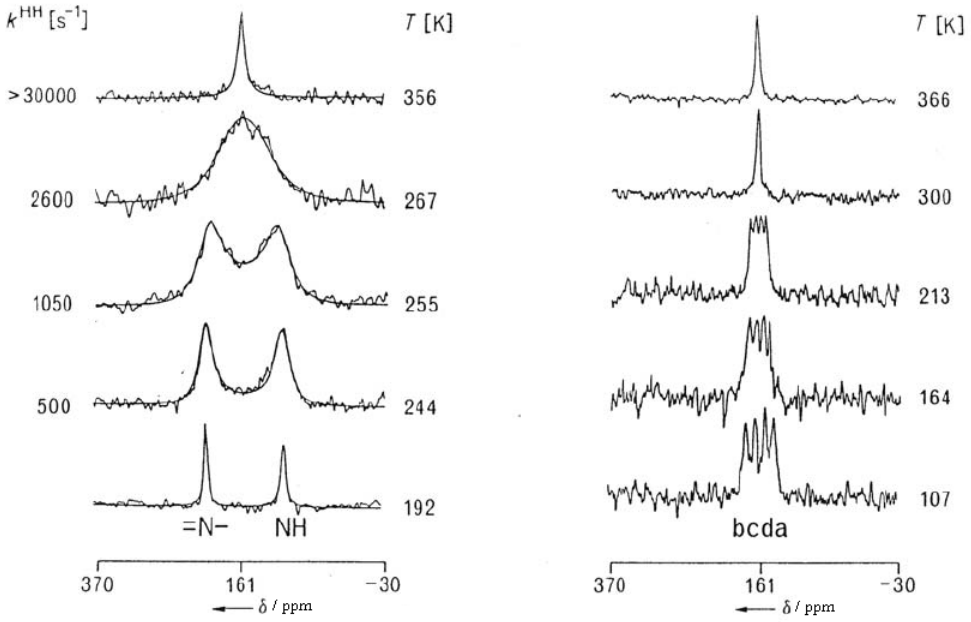

Figure 3.7: Solid state ^{15}N NMR chemical shift spectra of porphycene (right) and porphyrin (left), taken from Ref. [160].

3.2 Tunneling splitting in porphycene

Before studying the geometric and kinetic H/D isotope effects, we will provide some insight into the overall properties of the potential energy surface. Moreover, the tunneling splitting of porphycene and its isotopomers will be studied. First, the experimental technique, fluorescence spectrum, that has been used to measure the splitting in porphycene will be outlined in section 3.2.1. The Cartesian reaction surface Hamiltonian approach will be discussed in section 3.2.2, where the potential surface in terms of the reactive coordinates (of the proton motion) will be constructed and the ground state eigenfunctions and eigenvalues will be calculated. Further, a comparison between the mean field approximation and the exact calculation will be shown. The way to find the strongest coupled modes to the proton motion and how it will be incorporated into the potential energy surface will be briefly discussed. The five strongest coupled modes will be shown. In section 3.2.3 the Cartesian reaction plane will be studied in comparison with the Cartesian reaction surface approach. A correlation between the reaction plane coordinates and the hydrogen bond coordinates q_1 and q_2 will be discussed in section 3.2.3.

3.2.1 Fluorescence spectra as an evidence of tunneling splitting

Before going into the details of tunneling splitting in porphycene, we will give an overview of the experimental work done by Waluk and coworkers for porphycene using the fluorescence excitation spectroscopy. Waluk et al. [161, 162] have investigated the tunneling splitting of porphycene using the fluorescence excitation in an ultracold supersonic jet. They found that the fluorescence excitation spectra consist of doublets, see Fig. 3.8. The fluorescence spectrum, of non-deuterated species, shows a doublet separation of 4.4 cm^{-1} (the tunneling splitting in the lowest vibrational levels of the electronic ground state). This experimental value of the splitting will be used later for the comparison with our theoretical value.

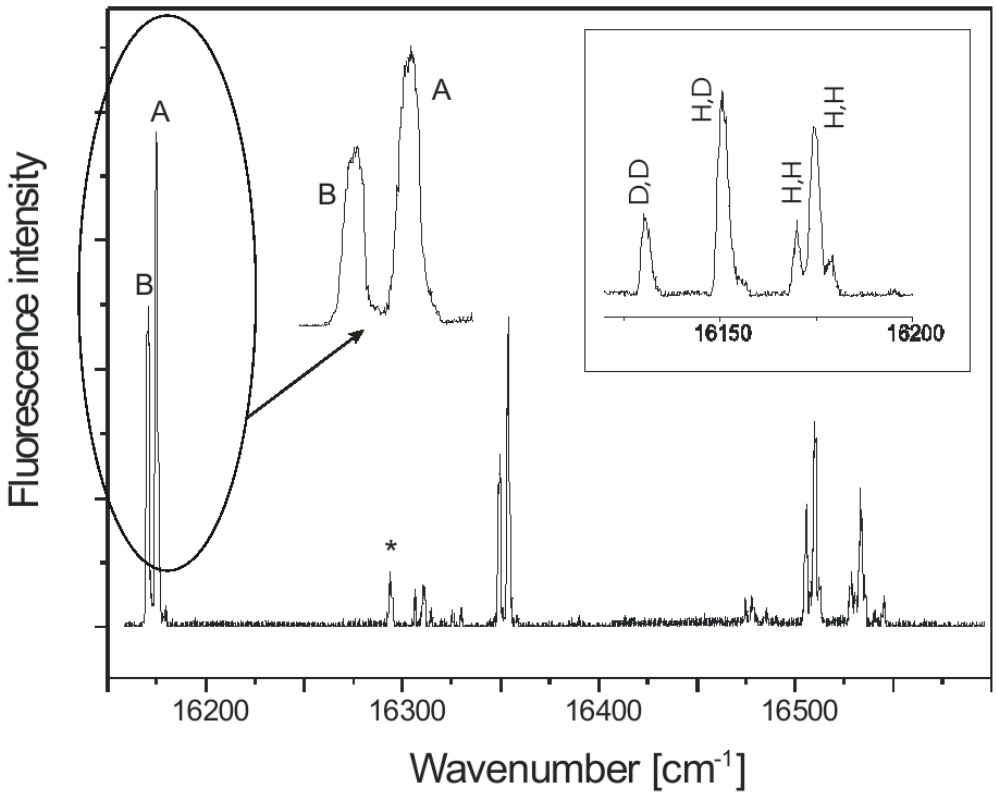

Figure 3.8: Fluorescence excitation spectra of porphycene isolated in a supersonic jet. Inset, the 0-0 transitions observed for undeuterated, singly and doubly deuterated porphycene. The peak marked with an asterisk corresponds to the complex of porphycene with water [162].

In contrast, porphyrin shows ”normal” single peak spectra corresponding to particular vibronic transitions [163]. The splitting in porphycene disappears upon replacing one or two inner protons with deuterons (This means that the splitting

becomes smaller than 0.1 cm^{-1} which is too small to be detected experimentally), this is shown in the upper right corner of Fig. 3.8. The peak marked by asterisk (Fig. 3.8) reveals a complex formation of water or alcohol with porphycene, i.e. adding water or alcohol to the sample results in concealing of the doublet structure. To distinguish the nature of the doublet components A and B depicted in Fig. 3.8, one can compare their relative intensities upon varying the conditions of cooling [162]. As shown in Fig. 3.9, the relative intensity of component B decreases with increasing the distance between the laser beam and the nozzle. On contrast, component A is not affected by changing the distance between the laser beam and the nozzle. Since increasing the distance from the nozzle leads to increasing the degree of cooling of the sample, the component B was assigned to be the hot band [162].

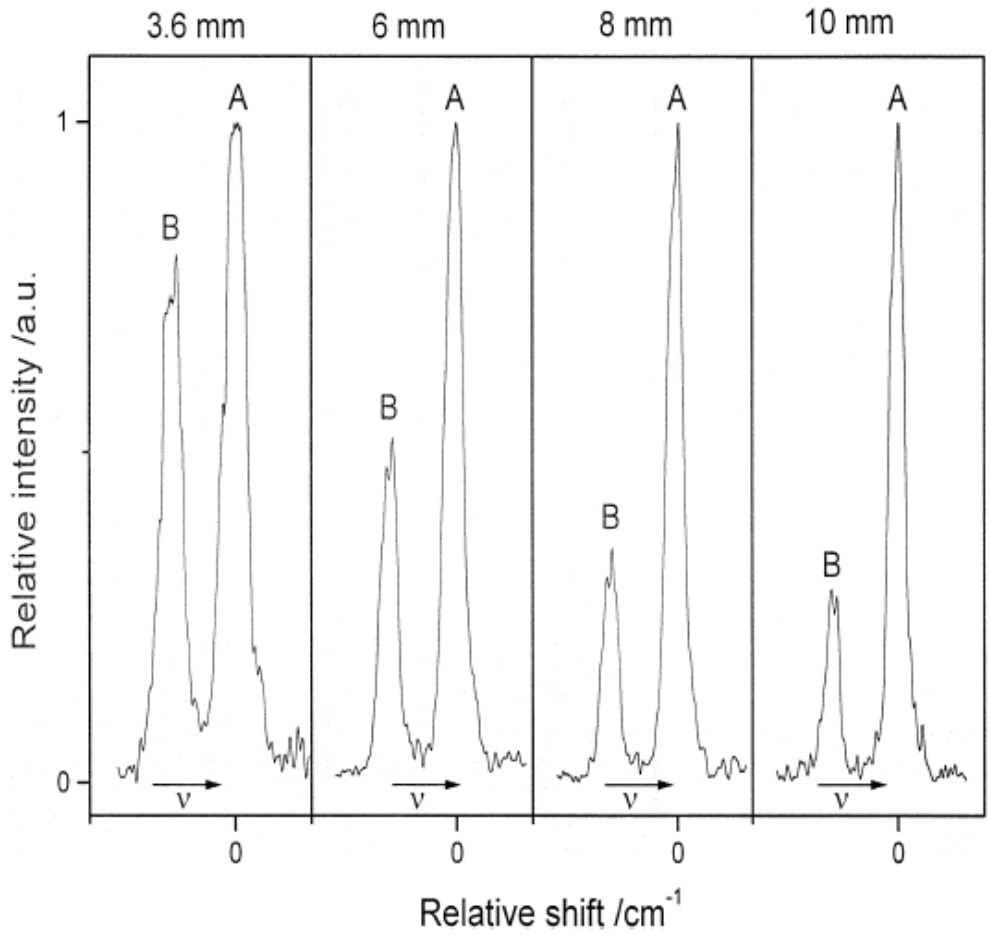

Figure 3.9: Relative intensities of the A and B components of the $S_0 - S_1$ electronic transition as a function of the distance between the nozzle and the laser beam [162].

Therefore, the hot nature of band B and the lack of doublet structure upon complexation with water (exempting because of symmetry lowering upon complex formation) provide a conclusive evidence that the splitting has been attributed to the ground state tunneling of the two inner hydrogen atoms.

In fluorescence spectra, one may observe three situations upon deuteration (assuming that the shift in the spectra (if exists) due to single and double deuteration is the same): a) The potentials (S_0 and S_1) are of the same shape, this means that the stabilization of the deuterated species will be the same in both potentials and no shift will be observed in the spectra; b) The potential S_1 is wider than S_0, this leads to a blue shift in the spectra since the stabilization will be larger in S_0 than in S_1 potential; c) The potential S_0 is broader than S_1, this means that the stabilization of the deuterated species will be larger in S_1 than in S_0 potential. Case c) leads to a red shift in the fluorescence spectra. In the case of porphycene, a red shift of the fluorescence excitation spectrum in single and double deuterated species is observed, see Fig. 3.8. Moreover, the shift is approximately the same per each substituted proton. This indicates that the stabilization of the deuterated species is larger in S_1 than in S_0 potential, i.e. the potential S_1 is steeper than S_0. The steepness of the potential S_1 indicates a smaller N-H bond length in the excited state, which implies that the hydrogen bond is weaker in the excited state. The molecule is most likely to expand upon excitation, and the cavity becomes larger. Further, the steepness of the S_1 potential leads to a higher barrier and in turn a smaller splitting than S_0 potential. This finding and the observation that all the vibronic peaks reveal the same separation of the doublet components, suggests that the observed value of 4.4 cm^{-1} can be assigned to ground state tunneling splitting (Fig. 3.10).

3.2.2 Cartesian reaction surface

A theoretical way to calculate the tunneling splitting is, first of all, to calculate the ground state potential energy surface of the system, and evaluate the ground state vibrational eigenvalues from which one can compute the tunneling splitting. In a first step we localize the stationary points (minima and saddle points) on the potential energy surface that are associated with the chemical reaction to be investigated. The stationary points (minima) for the concerted and stepwise double proton transfer reactions were determined and depicted in Fig. 3.11.

As has been shown in section 3.1, the reaction might proceed concertedly according to harmonic approximation. Therefore, for the time being, we intend to

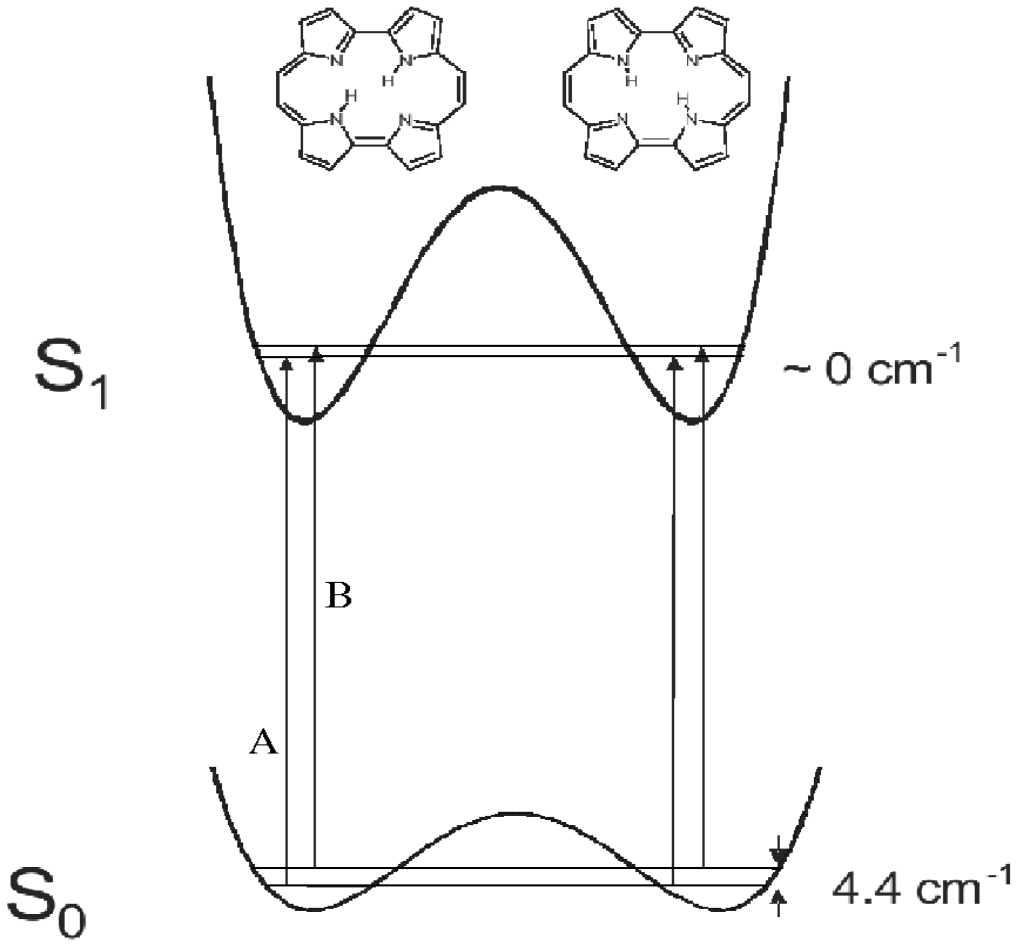

Figure 3.10: Schematic diagram represents the ground and lowest excited singlet state potential energy profiles along the tautomerization coordinate in porphycene [161] (Note: the molecular axis is rotated by 90° compared to Fig. 3.1).

study the overall properties of the potential energy surface of the concerted pathway (assuming the cis tautomer is not important for tunneling) and evaluated the tunneling splitting for such a reaction. In this respect, we used the Cartesian reaction surface Hamiltonian wherein we need to separate the total set of coordinates into those of the reactive hydrogen atoms which describe large amplitude concerted proton motion and those of the substrate as a harmonic skeleton modes Qs. The Cartesian system for the trans tautomer is depicted in Fig. 3.12.

Considering the flexible reference method (section 2.3.5), the reactive coordinates (x,y) for the concerted pathway are shown in Fig. 3.13. As shown in Fig. 3.13, the concerted proton transfer occurs in a curved pathway. The two hydrogen atoms are located closer to the y-axis for the minimum structure (trans) than the

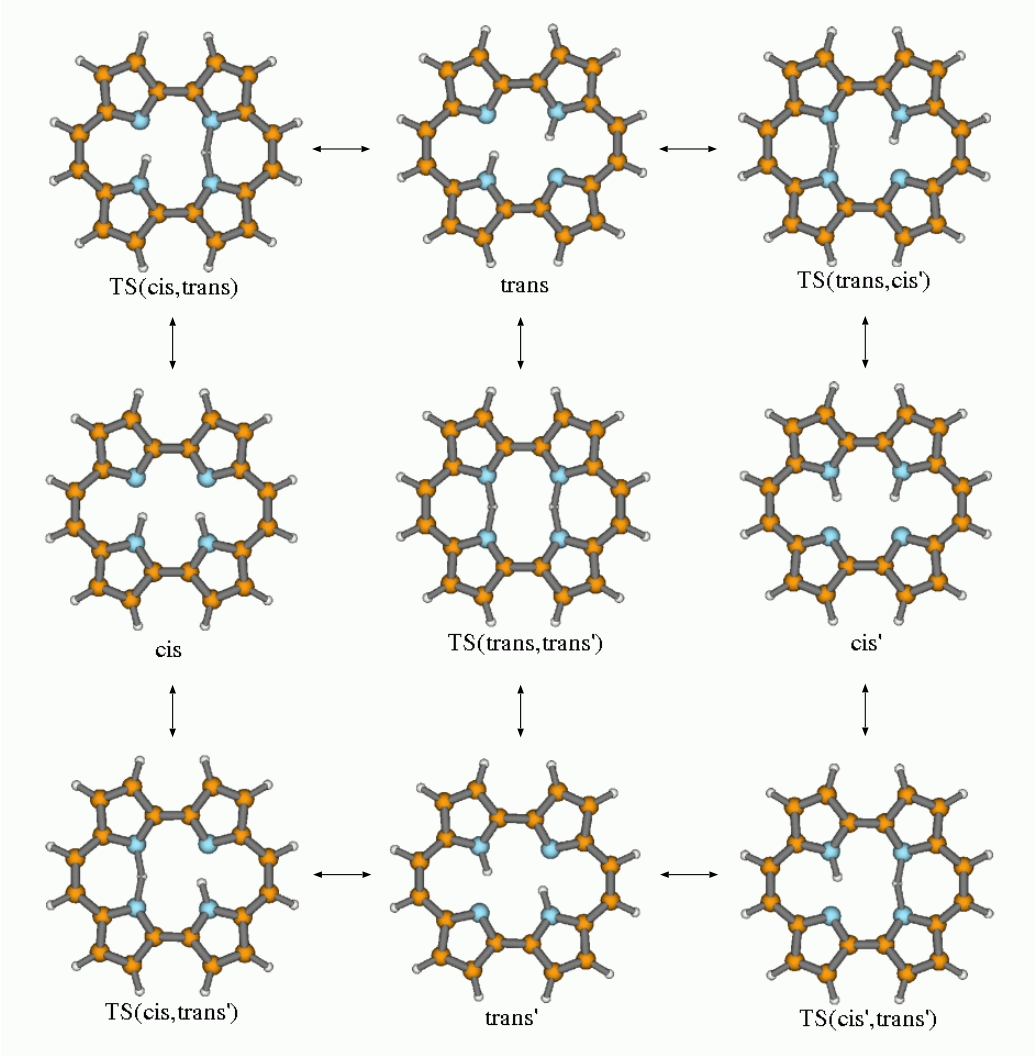

Figure 3.11: The stationary points (trans and cis isomers) obtained from density functional theory calculations with B3LYP/6-31G(d,p). The possible tautomerization pathways (stepwise and concerted) are also represented by arrows.

transition state. On going from one trans configuration to the other, the two hydrogens depart from the y-axis till having the maximum distance from the y-axis at the transition state and then get closer again for the other trans.

Since the geometries of the stationary points are planar, there is no force acting on the reactive hydrogen atoms along z-direction. Therefore we employed the x- and y-coordinates as reactive coordinates to describe the large amplitude motion of the hydrogen atoms.

The Cartesian surface Hamiltonian does not have any coupling for the kinetic energy, i.e. the different coordinates are only coupled via the potential energy

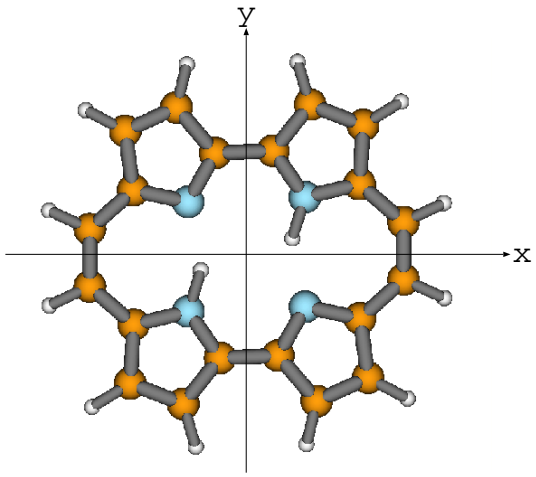

Figure 3.12: The Cartesian system of the trans geometry of the trans-porphycene. z-coordinate is perpendicular to the plane of the paper (Note: this presentation is rotated by 90° compared to Fig. 3.1).

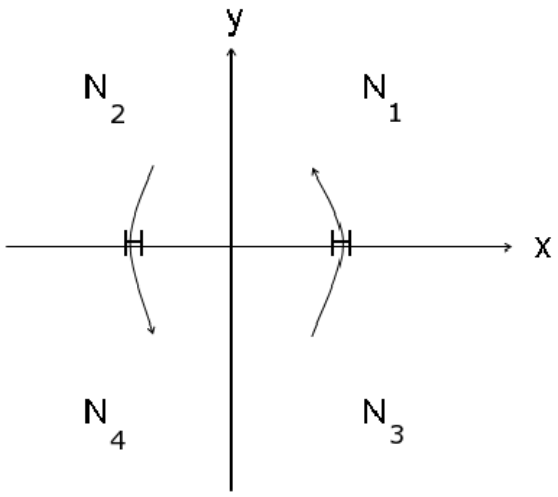

Figure 3.13: Sketch describing the reaction path for the concerted double proton transfer pathway. What is shown is the inner cavity of the double hydrogen bonds. Here a combination of x and y describes the simultaneous motion of both protons. The center of mass coincide with the origin of the coordinate system. Here x(N_1) = - x(N_2); x(N_3) = - x(N_4); y(N_1) = - y(N_3); and y(N_2) = - y(N_4). Since we have two moving protons, m_x = 2 H-mass and m_y = 2 H-mass. (Note: this presentation is rotated by 90° compared to Fig. 3.1).

surface for proton motion, $V_{eff}(x, y)$, the Hessian $\mathbf{K}(x, y)$ and the forces $\vec{f}(x, y)$.

The Hamiltonian then reads:

$$H_{CRS} = \frac{1}{2}\left(\frac{p_x^2}{m} + \frac{p_y^2}{m}\right) + V_{eff}(x,y) + \frac{1}{2}(P_Q^2 + \vec{Q}\mathbf{K}(x,y)\vec{Q}) - \vec{f}(x,y)\vec{Q}, \quad (3.1)$$

where m is twice the mass of the moving atom (proton or deuteron). The complete expression for the potential energy surface $V_{eff}(x,y)$ is given in Eq. (2.65). The large mass ratio between the hydrogen atoms and the substrate results in an insignificant change not only of the center of mass but also of the orientation of the principle axis of inertia during the proton transfer reaction. Therefore, one can neglect the coupling to the external motions (translation and rotation). As described in section 2.3.5, the full dimensionality of Eq. (3.1) can be simplified by considering the strongest coupled modes with the proton motion according to the value of the reorganization energy.

To construct the potential energy surface of this nuclear motion, we fixed the molecular structure of the trans tautomer in a Cartesian coordinate system where the center of mass of the molecule coincides with the origin of the Cartesian axes. The hydrogen motion along the path shown in Fig. 3.13 can be described by an elongation of NH bonds and a change of NNH angles. Therefore, changing the coordinates x and y (Fig. 3.13) simultaneously can be equivalent to changing r and θ coordinates depicted in Fig. 3.14.

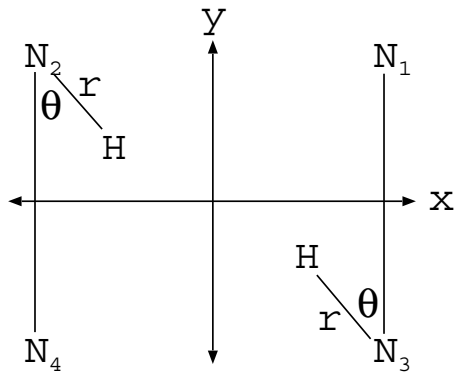

Figure 3.14: Sketch describing equivalent coordinates to the reactive coordinates (x,y). Here shown the cavity hosting the hydrogen bonds with the numbering system presented in Fig. 3.1.

Partial optimization as implemented in Gaussian98 program package [154] was used to construct the potential energy surface. Here we change r and θ coordinates and leave the rest of the molecular coordinates to relax to their new

equilibrium positions. We introduce r and θ instead of x and y because internal coordinates are required for the partial optimization in Gaussian program package. The calculated potential energy surface was composed of 219 points scattered in the range 0.8Å to 2.4Å for r and 10.4° to 18.5° for θ. Another 219 points were generated by symmetry and the total of 438 points were used in the potential energy fitting. The resulting potential energy surface was then fitted to a tenth order polynomial using the least-square fitting algorithm, see Fig. 3.15.

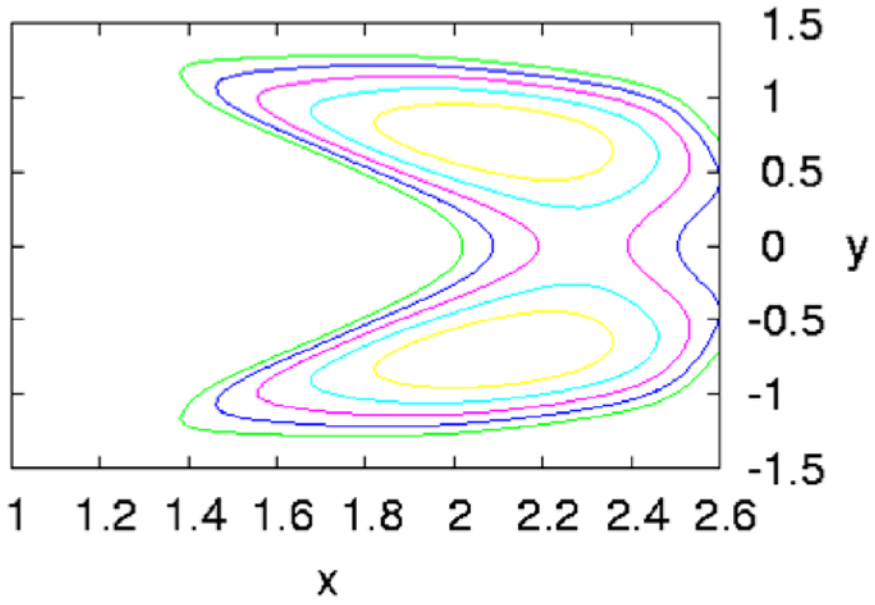

Figure 3.15: Contours plot of the two dimensional potential energy surface for the reactive coordinates (in atomic units) as defined in Fig. 3.13. The contour spacing: 0.0 to 0.5 in steps of 0.1 eV. The potential surface is a symmetric double well potential. The minimum energy path, connecting the two wells together and passing through the transition state, has a curved shape as represented in Fig. 3.13.

Assuming that the substrate modes adjust themselves adiabatically with the motion of the protons, i.e. the kinetic coupling is neglected (see section 2.3.5), the potential energy surface can then be reduced in terms of the reactive coordinates to the one depicted in Fig. 3.15.

Figure 3.15 shows contours plot of the two dimensional potential energy surface which is a symmetric double well potential, each well represents a certain trans configuration separated by a transition state which is 6.23 Kcal/mol higher than each minimum. Having this two dimensional potential we were able to calculate the two dimensional ground state eigenfunctions for porphycene and

deuterated porphycene as well as the ground state eigenvalues. Note that the deuteration has been done only for the inner protons. We used in the calculation of eigenfunctions and eigenvalues the multiconfiguration time-dependent Hartree approach [132] together with imaginary time relaxation [164] and diagonalization techniques. The calculations have been performed using the Heidelberg MCTDH program package [148]. Fast fourier transform collocation has been used as the discrete variable representation on grids (in atomic units): x [1.2:2.7] (32 points) and y [-1.5:1.5] (64 points). Five single particle functions for each coordinate were used. The effect of the mean-field approximation (only one single particle function per coordinate) is also investigated and depicted in Figs. 3.16.

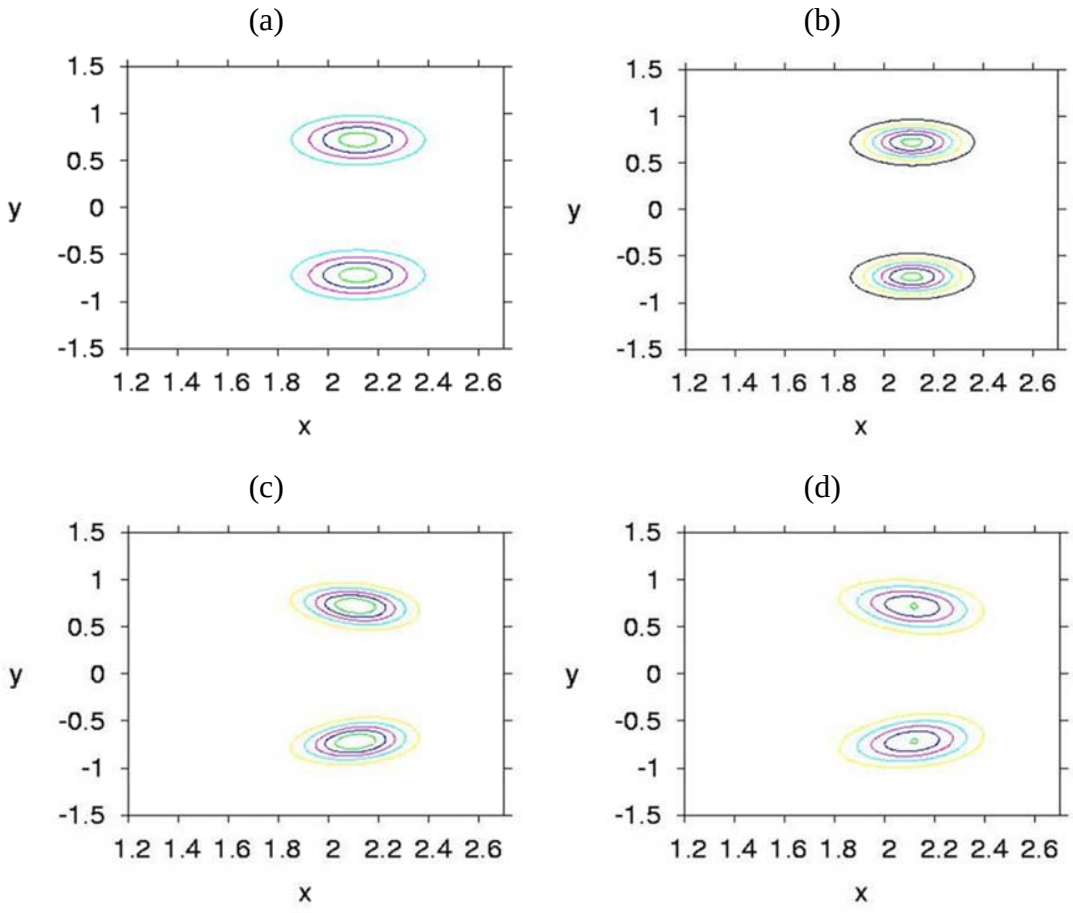

Figure 3.16: The ground state probability distribution functions for (a) porphycene and (b) deuterated porphycene (the mean-field approximation); (c) porphycene and (d) deuterated porphycene (numerical exact calculations). x and y are in atomic units.

It is obvious from Figs. 3.16 that the mean-field approximation is not a good approximation in this case because the ground state wave function does not fit

with the potential coupling yet contains two parallel lobes right above the two wells. On the other hand, by considering the numerically exact calculations, the two lobes of the ground state wave function will tilt accordingly to reproduce the potential coupling. This indicates that the motion of the wave function is most likely to follow the minimum energy path in case of exact calculations, while it makes a short cut motion in the mean-field approximation, even though it follows a higher energy path.

The tunneling splitting and the tunneling time were found to be (for porphycene) 1.2 cm^{-1} and 28 ps with relatively good agreement with the experimental value (4.4 cm^{-1}), see section 3.2.1 [161, 162]. With respect to deuterated porphycene, the tunneling splitting was 0.03 cm^{-1} and tunneling time was 1 ns. This tunneling splitting is a consequence of the overlap, in the barrier region, between localized wave functions in each well of the symmetric double well potential shown in Fig. 3.15, see section 1.1.2. The tunneling splitting of the normal species is larger than that of the deuterated ones because the wave function of the normal species is always higher in energy than that of the deuterated ones, i.e. wave function of the deuterated species is farther from the top of the barrier than that of normal ones, as indicated in section 1.1.2. There is no experimental value available for the splitting in the deuterated porphycene (the doublet structure disappears in the fluorescence spectra) because the calculated value is smaller than 0.1 cm^{-1} which is the minimum value that can be detected experimentally.

Selection of relevant modes

In proton transfer reactions, the coordinate(s) corresponding to the proton motion (in the present case x and y) is(are) usually coupled to certain reaction coordinates (e.g. normal modes), specially those describing the distance between the heavy atoms. This coupling is expressed also in an empirical q_1/q_2 model, see section 1.1.3. In the following we shall find the possible promoting or coupling modes, the terminology will be explained below.

As mentioned in section section 2.3.5 the reorganization energy, Eq. (2.69), corresponding to a certain mode can be used to identify the modes which couple strongly to the reaction coordinate of the proton motion. The reorganization energy, Eq. (2.69), is reflected in the substrate oscillator's displacement (Q^0) from their equilibrium value taken at the reference geometry. Let Q^0_{trans} be the displacement in the substrate modes on going from the reference structure (in the present case the transition state of the trans-trans interconversion) to one of the minimum

structures. The normal mode displacement of the strongest coupled mode is given in Fig. 3.17 (promoting mode). Mode v_{11}, Fig. 3.17, has the maximum value of Q^0_{trans} which is 104 $a_o(a.m.u)^{1/2}$. This symmetric mode (A_g) modifies the NN distance and has the strongest coupling with the proton motion and its wave number was found to be 301 cm^{-1}.

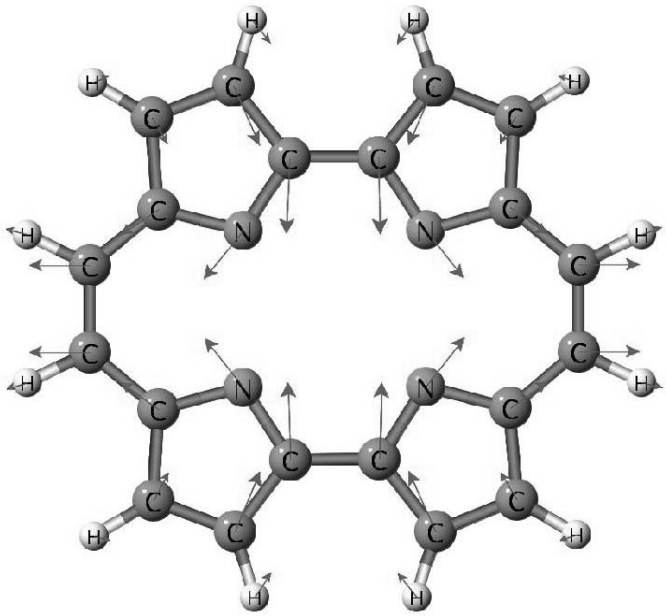

Figure 3.17: Mode v_{11} which has the strongest coupling to the reaction coordinates (promoting mode). It is a symmetric mode with wave number of 301 cm^{-1} and its Q^0_{trans} value is 104 $a_o(a.m.u)^{1/2}$.

The other relevant modes are depicted in Fig. 3.18. Some of them associated with the NN distance like the promoting modes v_{18} and v_{56} whose Q^0_{trans}s are 18 and 11 $a_o(a.m.u)^{1/2}$, respectively. Modes v_3 and v_{46} (whose Q^0_{trans} are 34 and 13 $a_o(a.m.u)^{1/2}$, respectively) describe the deformation of the structure as a result of the electronic reorganization which accompanies the proton motion (coupling modes). The wave numbers of these modes are as follows (in cm^{-1}): a) v_3 250; b) v_{18} 425; c) v_{46} 910; d) v_{56} 1075 and the corresponding symmetries are, respectively, B_{1g}, A_g, B_{1g} and A_g. Modes v_{11}, v_{18} and v_{56} facilitate the exchange of protons between nitrogen atoms, where they bring nitrogen atoms closer to one another and in turn affect the tunneling splitting. On the other hand, modes v_3 and v_{46} will enhance or suppress tunneling depending on their kind of deformation, i.e. the mode whose displacement facilitates the changes associated with the proton tunneling (for instance, electronic rearrangement) will enhance the tunneling and

vice versa.

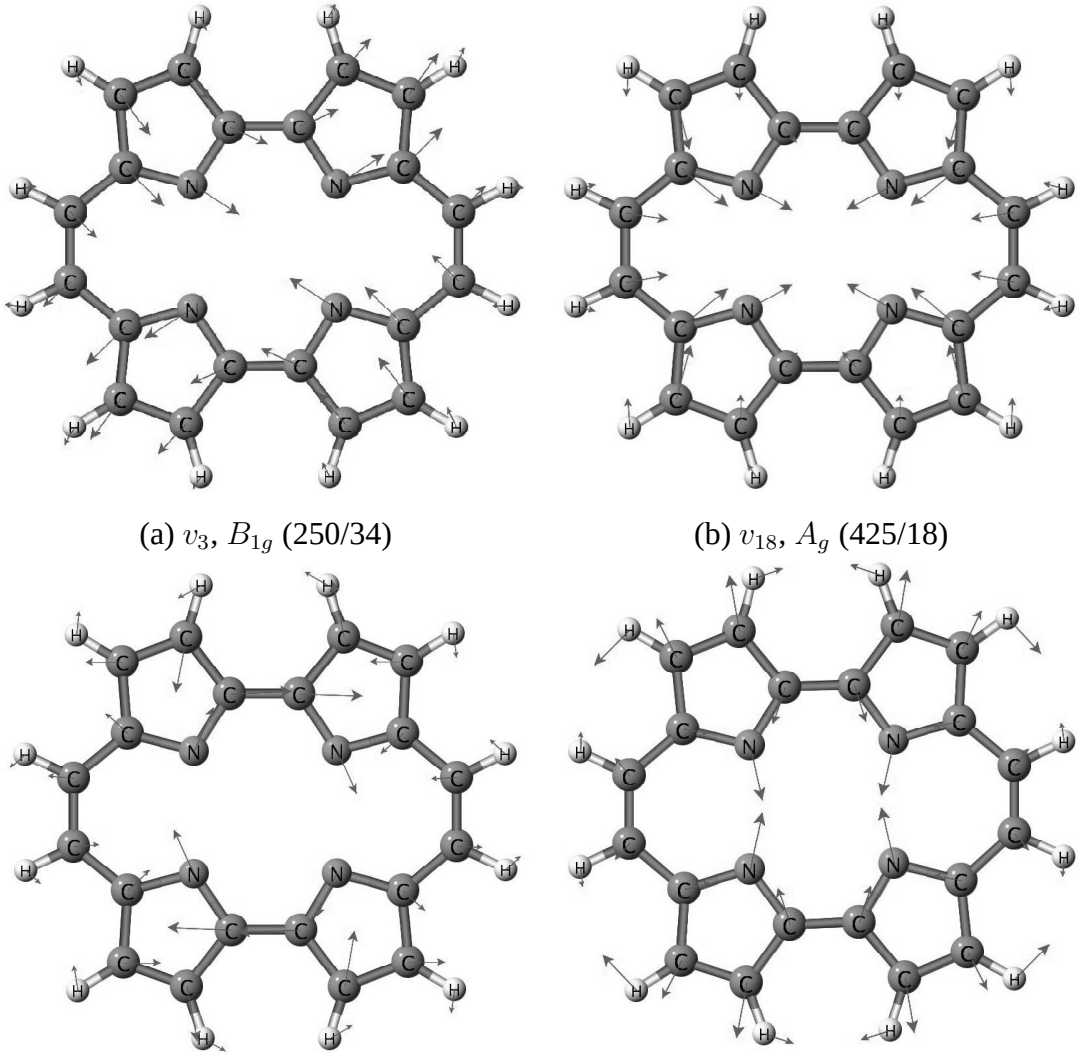

(a) v_3, B_{1g} (250/34)

(b) v_{18}, A_g (425/18)

(c) v_{46}, B_{1g} (910/13)

(d) v_{56}, A_g (1075/11)

Figure 3.18: The modes which couple strongly to the reactive coordinates, and their symmetries. Modes v_{18} and v_{56} are promoting modes, while modes v_3 and v_{46} are coupling modes. In paranthesis are given, respectively, the harmonic wave numbers and Q^0_{trans} values (in cm^{-1} and $a_o(a.m.u)^{1/2}$).

In the next section we will see how these coupled modes are covered by the so called Cartesian reaction plane coordinates.

3.2.3 Cartesian reaction plane

In this section, the collective reaction plane coordinates will be presented and correlated to the atomic reactive coordinates. Furthermore it will be discussed

how these Cartesian plane coordinates cover the relevant modes as well as the mode describing the reaction coordinate of the concerted mechanism. Finally, the direct relation between q_1/q_2 and d_1/d_2 will be discussed.

Let us consider the coordinate system, shown in Fig. 3.12, and see how to generate X_L from X_R, assuming that the structure depicted in Fig. 3.12 describes X_R. In order to obtain the geometry of X_L from the known geometry X_R, one can do the following: each of the atoms, located above the x-axis, are permutated with the corresponding ones below the same axis and then the whole molecule is rotated by 180°. These two structures are characterized by being unique up to an arbitrary rotation. In order to remove this arbitrariness, Nakamura [127] suggested to choose X_L and X_R such as to minimize $|X_R - X_L|$. Similarly, $|X_C - X_{TS}|$ should be minimized. The obtained vectors' displacements are depicted in Fig. 3.19.

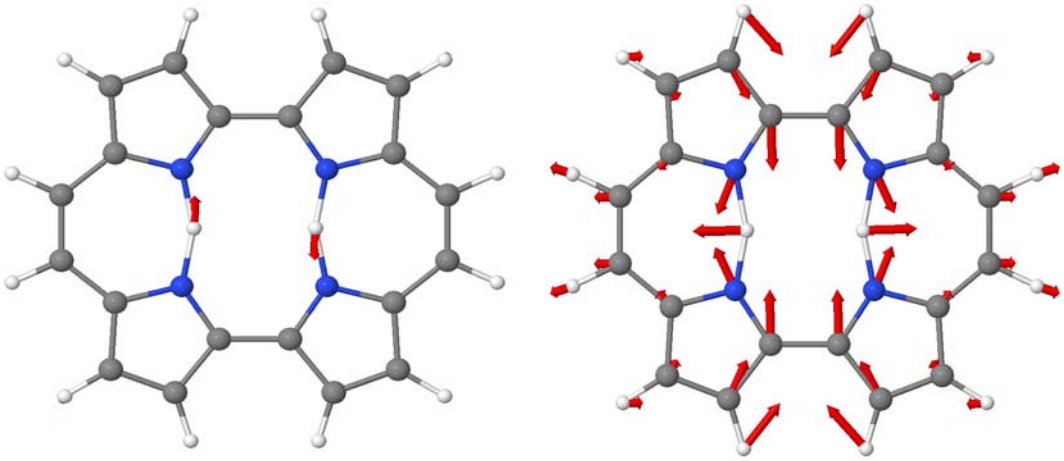

(a) d_1 (b) d_2

Figure 3.19: Collective atom displacement corresponding to direction (a) d_1-vector (antisymmetric) and (b) d_2-vector (symmetric), see Fig. 3.13.

Panel (a) of Fig. 3.19 represents a concerted motion of the two protons which corresponds to the straight line connecting both minima and the center geometry, see Fig. 3.13. Panel (b) represents the motion of the two protons in opposite directions along the x-axis from the saddle point to the center geometry, see Fig. 3.13. The small displacements for other atoms of the molecule is also considered but not shown in the figure. One can notice that d_2 has some displacements of other atoms as large as that of the moving protons, these displacements are accompanied with cavity shrinkage and expansion.

The coordinates, d_1 and d_2, can be correlated to the reactive coordinates de-

scribed in the previous section. The d_1 describes the motion along y-axis, see Fig. 3.12, this is directly related to the reactive y-coordinates, whereas the d_2 coordinate is associated with the proton motion along x-axis as well as motions of other atoms. The d_2 coordinate reflects a collective motion that is essentially the proton motion along x-direction which is related to the reactive x-coordinate described in the previous section. Moreover, the collective coordinate d_2 describes the motion of the nitrogen atoms in such a way as to enlarge or shrink the cavity hosting the two hydrogen bonds which is also accompanied with other motions of atoms in the rings as well as the outer hydrogens.

Another interesting observation that d_1 and d_2 correlate not only to the reactive coordinates, x and y, but also to the strongly coupled modes to these reactive coordinates. The d_2 coordinate covers the strongest coupled mode v_{11} (Fig. 3.17). This is reflected in the projection of d_2 on v_{11} $(\vec{Q}_{11} \cdot \vec{d}_2)$ which is evaluated to be 0.85. This is not surprising since d_2 has promoting character by symmetry. Likewise, d_1 covers the reaction coordinate, obtained from ab initio calculations, which has an imaginary frequency in case of concerted mechanism, see Fig. 3.20.

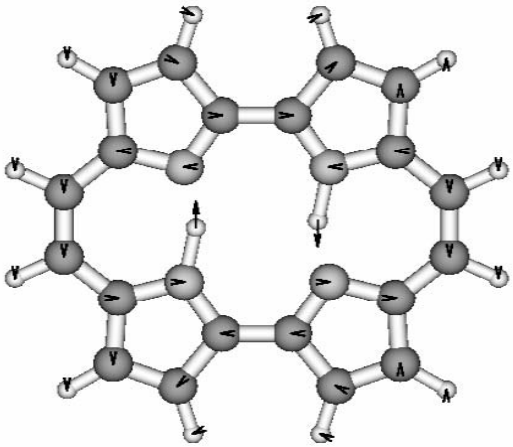

Figure 3.20: The mode with imaginary frequency for the transition state of the trans-trans interconversion.

So far, we have discussed how the collective reaction plane coordinates (d_1 and d_2) cover the atomic reactive coordinates (x and y) and the strongest coupled mode v_{11}. In addition, one may ask whether the reaction plane coordinates, d_1 and d_2, correlate to the empirical q_1 and q_2 or not. To answer this question, we recall the definition of q_1 and q_2, that are the deviation of the proton from the center of the hydrogen bond and the distance between the heavy atoms hosting the hydrogen bond, respectively. In other words q_1 can be considered as the tunneling

coordinate which corresponds to d_1 as described above. Regarding the heavy atoms, d_2 describes how much the heavy atoms' distances expand or shrink on going from the center geometry to the transition state which in turn reflects the distance between the heavy atoms, i.e. related to q_2.

3.3 Anharmonic potential energy surface

Now comes the study of certain features of the potential energy surface around a specific structure (trans tautomer). In this section we consider the anharmonicity of the potential energy surface in the vicinity of the trans geometry (see Fig. 3.1) to probe the properties of the nuclear ground state wave function. Therefore, the influence of the tunneling between the trans minima in the potential energy surface is neglected. Indeed, since the tunneling splitting, as determined from fluorescence excitation spectra, is relatively small (4.4 cm^{-1}) [162], there should be only a marginal effect on the shape of the local probability distribution. This is supported by Fig. 3.16. Since we are dealing with the electronic ground state ($el = 0$), we will drop the index el from the potential energy surface.

The resulting set of normal mode coordinates presented in section 3.1, $\{ Q_i \}$, and conjugate momenta, $\{ P_i \}$, can be used to express the Hamiltonian in Watson form (neglecting vibration-rotation couplings) [165]:

$$H = \sum_{i=1}^{3N-6} \frac{P_i^2}{2} + V(Q_1, Q_2, ..., Q_{3N-6}), \tag{3.2}$$

where $V(Q_1, Q_2, ..., Q_{3N-6})$ is the full-dimensional potential energy surface. As discussed in section 2.3, the calculation of the full-dimensional potential energy surface is only feasible for very small systems such as triatomic molecules. In contrast, for systems like porphycene it is impossible to get a full-dimensional potential energy surface without approximations. The importance of the correlation between the normal modes is likely to decrease with increasing the number of correlated modes, thus, it is reasonable to expand the full-dimensional potential energy surface $V(Q_1, Q_2, ..., Q_{3N-6})$ in terms of correlated and uncorrelated contributions as [166]

$$\begin{aligned} V(Q_1, Q_2, ..., Q_{3N-6}) = &\sum_i V_i^{(1)}(Q_i) + \sum_{i<j} V_{ij}^{(2)}(Q_i, Q_j) \\ &+ \sum_{i<j<k} V_{ijk}^{(3)}(Q_i, Q_j, Q_k) + \dots \end{aligned} \tag{3.3}$$

The summations run over all normal modes as singles, distinct pairs, triples, etc. The terms $V_i^{(1)}(Q_i)$, $V_{ij}^{(2)}(Q_i, Q_j)$, $V_{ijk}^{(3)}(Q_i, Q_j, Q_k)$ ... are the uncorrelated, two-mode correlations, three-mode correlations, ... and so forth. In other words, $V_i^{(1)}(Q_i)$ corresponds to one-dimensional potential energy curve of the displaced equilibrium structure (trans tautomer) along a specific normal mode i while the other normal modes are frozen at their equilibrium values, the $V_{ij}^{(2)}(Q_i, Q_j)$ contains the coupling between two modes i and j, $V_{ijk}^{(3)}(Q_i, Q_j, Q_k)$ contains the coupling between three modes i, j and k, etc. The potential $V^{(2)}(Q_i, Q_j)$ can be calculated as follows: the equilibrium geometry (trans tautomer) is displaced along two specific modes, and the corresponding potential energy is then evaluated for the displaced structure using single point calculation technique implemented in Gaussian03 program package [155]. One has to notice that the potential $V^{(2)}(Q_i, Q_j)$ includes the uncorrelated terms $V_i^{(1)}(Q_i)$, where $V^{(2)}(Q_i, Q_j) = V_i^{(1)}(Q_i) + V_j^{(1)}(Q_j) + V_{ij}^{(2)}(Q_i, Q_j)$, i.e. when two modes potentials $V^{(2)}(Q_i, Q_j)$ and $V^{(2)}(Q_j, Q_k)$ are calculated, the one dimensional potential energy $V_j^{(1)}(Q_j)$ should be subtracted from one of the two modes potentials. Calculation of $V^{(3)}(Q_i, Q_j, Q_k)$ or higher order couplings is computationally demanding for large systems. Therefore, one may employ some approximation to deal with large systems as porphycene.

3.3.1 From full-dimensionality to reduced dimensionality

Here we see how to deal with the highly demanding full-dimensionality by introducing some approximations. The coupling between different modes is also studied and how this coupling is reflected in the anharmonicity of the potential energy surface. Porphycene has 108 normal modes that make it impossible to build up the exact full-dimensional potential energy surface. Therefore, a careful selection of the degrees of freedom, which are relevant for the description of the primary and secondary geometric isotope effect, is required. The primary geometric isotope effect can be captured by taking into account those modes which are related to the N-H bond motion, such as the symmetric ($Q_1^{HH/DD}$) and antisymmetric ($Q_2^{HH/DD}$) N-H(D) stretching vibrations whose normal mode displacements are shown in Fig. 3.21. The Q_1^{HH} and Q_2^{HH} are modes number 95 and 96, respectively, as mentioned in Table 3.2.

In order to identify the modes which are strongly coupled to the stretching vibrations we have displaced the minimum trans structure (Fig. 3.1) along $Q_1^{HH/DD}$ and $Q_2^{HH/DD}$ by $\pm$ 5 a_o(a.m.u)$^{1/2}$, and calculated the corresponding Hessian ma-

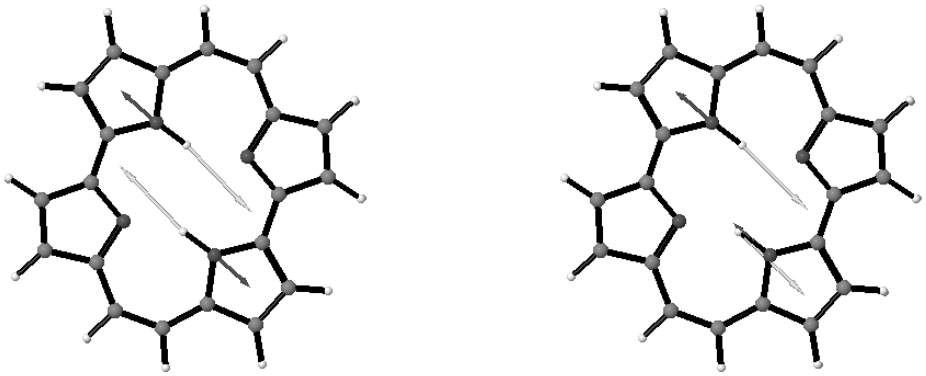

(a) $Q_1^{HH/DD}$ (2891/2154) (b) $Q_2^{HH/DD}$ (2892/2155)

Figure 3.21: The normal mode displacement vectors corresponding to the N-H/N-D stretching vibrations for the HH and DD cases. (a) symmetric stretch; (b) asymmetric stretch. In paranthesis the harmonic wave numbers are given (HH/DD in cm^{-1}).

trix, $\mathbf{K}(Q_{1/2}^{HH/DD})$, as well as the force, $f_j(Q_{1/2}^{HH/DD})$, acting on the remaining modes Q_j at this non-equilibrium position. The higher the value of the force is, the stronger the coupling with the stretching displaced modes. This force leads to displacement according to Eq. (2.68). The important quantity (Q^0) that measures the coupling to the displaced modes is the displacement of the other modes from their equilibrium position. Table 3.5/3.6 and 3.7/3.8 shows the modes which couple to the displaced $Q_1^{HH/DD}$ and $Q_2^{HH/DD}$ modes and has the highest forces, respectively, as well as their wave numbers and the displacements of the coupled modes (Q^0) which exceed 0.20 a_o(a.m.u)$^{1/2}$.

Inspecting Tables 3.5 to 3.8 reveals that the strongest coupled mode (largest displacement) with the stretching modes $Q_1^{HH/DD}$ and $Q_2^{HH/DD}$ is mode number 7 ($Q_3^{HH/DD}$). The displacement of the other modes from their equilibrium positions as reflected in Q^0 values of tables 3.5 to 3.8 is very small as compared to that of $Q_3^{HH/DD}$. The strongest coupled mode mode, $Q_3^{HH/DD}$, (see Fig. 3.22) is then incorporated into the potential energy surface, eqn. (3.3). Notice that this mode (low frequency mode) is associated with the modification of the N-N distance in the cavity and then causes a symmetric contraction or elongation of the two hydrogen bonds, i.e. it is strongly related to the secondary geometric H/D isotope

No.	$\widetilde{\omega}$ (cm^{-1})	Q^0 (a$_o$(a.m.u)$^{1/2}$)	No.	$\widetilde{\omega}$ (cm^{-1})	Q^0 (a$_o$(a.m.u)$^{1/2}$)
7	196	-5.98	55	999	-0.38
16	370	0.30	57	1016	-0.21
20	490	-0.25	72	1310	0.33
23	610	-0.30	83	1474	0.31
29	673	-0.38	87	1524	0.23
40	835	0.40	88	1554	0.22
43	881	-0.26	94	1643	-0.26

Table 3.5: The normal modes coupled to the displaced mode $Q_1^{HH} = 5$a$_o$(a.m.u)$^{1/2}$, their wave numbers and their displacement from the equilibrium position.

No.	$\widetilde{\omega}$ (cm^{-1})	Q^0 (a$_o$(a.m.u)$^{1/2}$)
7	194	6.22
16	370	0.32
20	486	0.40
23	609	0.42
30	664	-0.53
41	830	0.67
45	877	0.39
53	954	-0.65
56	985	-0.29
65	1159	0.21

Table 3.6: The normal modes coupled to the displaced mode $Q_1^{DD} = 5$a$_o$(a.m.u)$^{1/2}$, their wave numbers and their displacement from the equilibrium position.

No.	$\widetilde{\omega}$ (cm^{-1})	Q^0 (a$_o$(a.m.u)$^{1/2}$)	No.	$\widetilde{\omega}$ (cm^{-1})	Q^0 (a$_o$(a.m.u)$^{1/2}$)
7	186	-9.63	57	1016	-0.31
20	491	-0.34	60	1083	-0.22
23	610	-0.49	72	1309	0.47
29	674	-0.48	83	1485	0.36
40	832	0.62	87	1530	0.27
43	877	-0.51	88	1560	0.27
50	947	-0.32	94	1657	-0.30
55	994	-0.61	96	2961	0.47

Table 3.7: The normal modes coupled to the displaced mode $Q_2^{HH} = 5$a$_o$(a.m.u)$^{1/2}$, their wave numbers and their displacement from the equilibrium position.

No.	$\widetilde{\omega}$ (cm^{-1})	Q^0 (a$_o$(a.m.u)$^{1/2}$)	No.	$\widetilde{\omega}$ (cm^{-1})	Q^0 (a$_o$(a.m.u)$^{1/2}$)
7	184	9.98	51	918	0.31
15	344	0.54	65	1163	0.21
20	487	0.55	53	954	-0.86
23	608	0.65	56	982	-0.49
30	665	-0.68	57	1011	0.22
41	823	1.02	60	1051	0.44
42	829	0.21	67	1203	0.21
45	870	0.69	70	1239	0.27
46	890	-0.33	83	1455	0.25

Table 3.8: The normal modes coupled to the displaced mode $Q_2^{DD} = 5$a$_o$(a.m.u)$^{1/2}$, their wave numbers and their displacement from the equilibrium position.

effect[1]. Since Cartesian reaction plane coordinate d_2 (section 3.2.3) represents the modification motion of the N-N distance as a part of its collective motion, the mode $Q_3^{HH/DD}$ is then covered by d_2. The potential energy surface was determined up to two-mode correlation terms [166] (the first two terms of the right hand side of Eq. (3.3)) by displacing the equilibrium geometry along each two modes. We used 171 points for each two mode potential.

$$\begin{aligned} V(Q_1^{HH/DD}, Q_2^{HH/DD}, Q_3^{HH/DD}) \\ &= V_1^{(1)}(Q_1^{HH/DD}) + V_2^{(1)}(Q_2^{HH/DD}) + V_3^{(1)}(Q_3^{HH/DD}) \\ &\quad + V_{12}^{(2)}(Q_1^{HH/DD}, Q_2^{HH/DD}) + V_{13}^{(2)}(Q_1^{HH/DD}, Q_3^{HH/DD}) \\ &\quad + V_{23}^{(2)}(Q_2^{HH/DD}, Q_3^{HH/DD}), \end{aligned} \tag{3.4}$$

Notice that Eq. (3.4) might include higher order couplings between each two modes like, for instance, $V^{(2)} \sim Q_1^n Q_2^m$.

In contrast to Cartesian reaction surface Hamiltonian (section 3.2.2), the normal mode coordinates are mass-weighted and, therefore, this procedure is followed for the normal species (HH) and the double H/D isotope substitution case (DD). The resulting one- and two-dimensional potentials are then fitted to tenth-order polynomials using the least-square fitting algorithm.

In the following we will discuss how to refine this model in a sense such as to include more modes that are coupled to the stretching vibrations via calculations of the third-order force constants, K_{ijk}, which also provide a means for including higher order correlations. Since we restrict our investigation to small changes of the nuclear degrees of freedom, the anharmonic force field approach provides a good approximation to the potential energy surface. The set of coupled modes (symbolized for the time being as Q_c) will contribute their harmonic (K_{cc}) and

[1]Gil et al. found that the 180 cm^{-1} vibration is promoting the tautomerization in bare porphycene in the electronic excited state. This has been proved by observing that the activation energy for the reaction in S_1, obtained from the Arrhenius plot, corresponds exactly to this value (they determined the reaction rate as a function of temperature by stationary and time-resolved fluorescence anisotropy measurements [167]). These results have been confirmed by large tunneling splitting for this mode in S_0, larger than those for other vibronic levels (these measurements have been obtained in jets and nanohelium droplets).

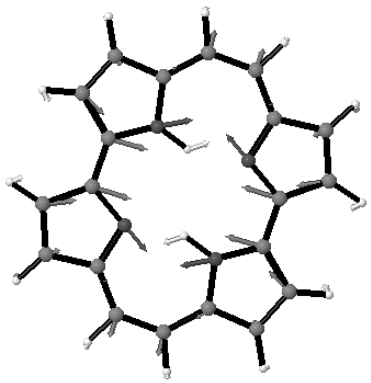

$Q_3^{HH/DD}$ (187/185)

Figure 3.22: The normal mode displacement vector corresponding to the change in the NN distance for the HH and DD cases. In paranthesis the harmonic wave numbers are given (HH/DD in cm^{-1}).

the pure/mixed third order force constants to the potential energy surface as

$$\begin{aligned} V(\mathbf{Q}) = & \sum_{i=1}^{3} V_i^{(1)}(Q_i) + \sum_{i=1}^{3}\sum_{i<j}^{3} V_{ij}^{(2)}(Q_i, Q_j) + \frac{1}{2}\sum_{i=1}^{3}\sum_{c} K_{iic} Q_i^2 Q_c \\ & + \frac{1}{2}\sum_{i=1}^{3}\sum_{c} K_{icc} Q_i Q_c^2 + \sum_{i=1}^{3}\sum_{i<j}^{3}\sum_{c} K_{ijc} Q_i Q_j Q_c \\ & + \frac{1}{2}\sum_{c} K_{cc} Q_c^2 + \frac{1}{6}\sum_{cc'c''} K_{cc'c''} Q_c Q_{c'} Q_{c''}, \end{aligned} \tag{3.5}$$

where i and j change from 1 to 3 and represent modes $Q_1^{HH/DD}$,$Q_2^{HH/DD}$ and $Q_3^{HH/DD}$, see Figs. 3.21 and 3.22. The first two terms of the right hand side of Eq. (3.5) can be calculated on a numerical grid, as shown in Eq. (3.4).

Now, to calculate the third order force constants, K_{ijk}, one can use the finite difference approach [168]. This approach requires calculations of the analytical Hessian for a displaced geometry along a single mode, for instance $Q_1^{HH/DD}$, then the third order force constant can be calculated using Eq. (2.59). In the present case, K_{ij}^{+} and K_{ij}^{-} are the second derivatives matrices corresponding to the displaced geometries along mode $Q_1^{HH/DD}$ in the positive and negative directions, respectively. The modes with the highest K_{ij1} absolute value will contribute into the potential energy surface, Eq. (3.5) as Q_c.

In order to calculate the K-terms of Eq. (3.5), one has to check the convergence of calculating the third order force constants. If the convergence is attained,

the results should not depend on the step size [168]. Therefore, to find the optimal displacement, one has to displace Q_1^{HH} and Q_2^{HH} from the equilibrium geometry, e.g., by 0.02 and 0.03 (dimensionless) in positive and negative directions (these are values typically suggested in Ref. [169]). The analytical Hessian for this displaced structure is then calculated. The corresponding cubic K-terms can be evaluated from Eq. (2.59). The third order K-terms of the stretching modes and the low frequency mode are shown in Table 3.9. The difference in the third order force constant of the two displacements (0.02 and 0.03) is about 0.7 $h{\cdot}c{\cdot}cm^{-1}$ and 0.5 $h{\cdot}c{\cdot}cm^{-1}$ for Q_1^{HH} and Q_2^{HH}, respectively. In addition, we displaced the equilibrium geometry along Q_3^{HH} by 0.03 in positive and negative directions and calculated the analytical Hessian for the displaced structure. The third order K-terms (with the stretching modes) was then calculated to be K_{113} = 128.0 $h{\cdot}c{\cdot}cm^{-1}$ and K_{223} = 124.1 $h{\cdot}c{\cdot}cm^{-1}$. These values differ from the corresponding cubic K-terms of the displaced stretching modes by only 1.0 and 0.3 $h{\cdot}c{\cdot}cm^{-1}$, respectively. Table 3.9 and the evaluated cubic K-terms of the displaced Q_3^{HH} reveal that 0.03 displacement is a reasonable displacement for the calculation of the third order force constants.

Displacement	K_{113} ($h{\cdot}c{\cdot}cm^{-1}$)	K_{223} ($h{\cdot}c{\cdot}cm^{-1}$)
0.02	128.3	124.9
0.03	129.0	124.4

Table 3.9: Conversion test for Q_3^{HH} : the third order K-terms for different displacement values of the stretching modes Q_1^{HH} and Q_2^{HH}.

Now, the coupled mode(s), Q_c, has to be specified. This was achieved by displacing the equilibrium geometry along $Q_1^{HH/DD}$ by 0.03 and calculating the third order force constants. Carefull inspection of the third-order force constant values leads to identification of the coupled modes to the stretching vibrations. The third-order force constants which contribute in the potential energy surface are given in Table 3.10.

It turns out that in both cases, HH and DD, there is an important coupled mode ($Q_4^{HH/DD}$) at around 900 $h{\cdot}c{\cdot}cm^{-1}$ of B_u symmetry whose displacement vectors are shown in Figs. 3.23a (HH) and 3.23b (DD). One can notice that the third order coupling between the stretching modes and this mode is very large compared to the two-mode coupling reflected in the oscillator's displacement upon displacement of each of the stretching modes. As for $Q_1^{HH/DD}$ displacement, these modes

are not included in Tables 3.5 and 3.6 due to their zero oscillator's displacement. On the other hand, they have negligible values in case of $Q_2^{HH/DD}$ as shown in Tables 3.7 and 3.8. (mode number 50 (HH) and 51 (DD)). The reason is that displacement along this mode will lower the symmetry and allow for asynchronous contraction/elongation of the two hydrogen bonds. This lowering in symmetry might be compensated by considering both stretching modes (of different symmetries) in the coupling with $Q_4^{HH/DD}$, in accord with symmetry rules[2] as reflected in Table 3.10. There are no diagonal third-order force constants for these modes, however, there is a particularly strong three-mode correlation with the stretching vibrations, K_{124}^{HH} = -224.36 $h{\cdot}c{\cdot}cm^{-1}$ and K_{124}^{DD} = -196.66 $h{\cdot}c{\cdot}cm^{-1}$, as well as a weaker coupling with the asymmetric stretching and the low-frequency vibration, K_{234}^{HH} = -34.58 $h{\cdot}c{\cdot}cm^{-1}$ and K_{234}^{DD} = -24.23 $h{\cdot}c{\cdot}cm^{-1}$. All other couplings do not exceed 10 $h{\cdot}c{\cdot}cm^{-1}$, see Table 3.10. Keeping the harmonic approximation for mode $Q_4^{HH/DD}$ and combining it with the explicit two-mode potential for modes $Q_1^{HH/DD}$, $Q_2^{HH/DD}$ and $Q_3^{HH/DD}$ as well as the third-order anharmonic couplings mentioned before, we arrive at a 4D model for the HH and DD cases. The potential energy surface will then read

$$
\begin{aligned}
V(&Q_1^{HH/DD},Q_2^{HH/DD},Q_3^{HH/DD},Q_4^{HH/DD}) \\
&= V^{(1)}(Q_1^{HH/DD}) + V^{(1)}(Q_2^{HH/DD}) + V^{(1)}(Q_3^{HH/DD}) \\
&\quad + V^{(2)}(Q_1^{HH/DD},Q_2^{HH/DD}) + V^{(2)}(Q_1^{HH/DD},Q_3^{HH/DD}) \\
&\quad + V^{(2)}(Q_2^{HH/DD},Q_3^{HH/DD}) + \frac{1}{2}K_{44}Q_4^{HH/DD}Q_4^{HH/DD} \\
&\quad + \frac{1}{2}K_{144}Q_1^{HH/DD}Q_4^{HH/DD}Q_4^{HH/DD} + \frac{1}{2}K_{344}Q_3^{HH/DD}Q_4^{HH/DD}Q_4^{HH/DD} \\
&\quad + K_{124}Q_1^{HH/DD}Q_2^{HH/DD}Q_4^{HH/DD} + K_{234}Q_2^{HH/DD}Q_3^{HH/DD}Q_4^{HH/DD},
\end{aligned}
\tag{3.6}
$$

where $Q_1^{HH/DD}$, $Q_2^{HH/DD}$, $Q_3^{HH/DD}$ and $Q_4^{HH/DD}$ are shown in Figs. 3.21, 3.22 and 3.23, respectively.

For the asymmetric substitution case, HD, we followed the same strategy. First, an explicit two-mode correlation potential has been obtained comprising the two local stretching vibrations Q_1^{HD} and Q_2^{HD} and the strongly coupled low-frequency mode Q_6^{HD}, see Fig. 3.24. The oscillators' displacements coupled to Q_1^{HD} and Q_2^{HD} which exceed 0.20 a_o(a.m.u)$^{1/2}$ are depicted in Tables 3.11 and

[2] As a symmetry rule, the Hamiltonian should be totally symmetric. Therefore, the direct product of the displacement vectors, considered in the coupling, has to be taken into account to keep the Hamiltonian symmetric.

	HH	DD
ijk	K_{ijk} ($h{\cdot}c{\cdot}cm^{-1}$)	K_{ijk} ($h{\cdot}c{\cdot}cm^{-1}$)
144	10.39	1.01
344	0.94	2.25
124	-224.36	-196.66
234	-34.58	-24.23

Table 3.10: The values of the third-order force constant which contribute in the anharmonic potential energy surface for the HH and DD cases, according to the symmetry rules. The others should not contribute in the potential energy surface due to symmetry rules and their values do not exceed 1 $h{\cdot}c{\cdot}cm^{-1}$.

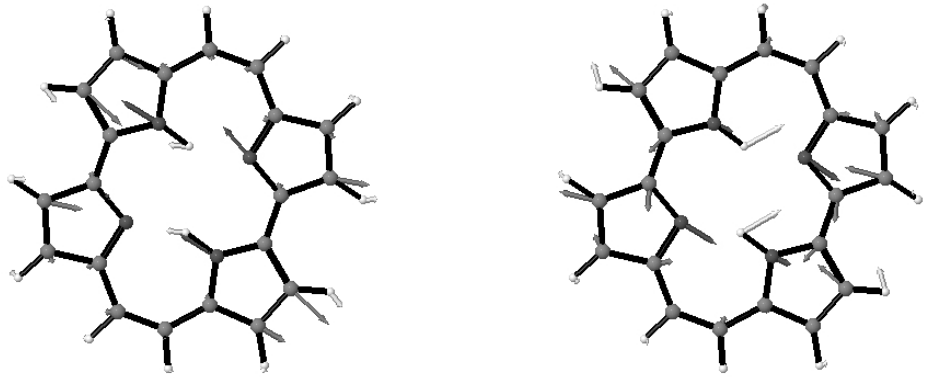

(a) Q_4^{HH} (947/B_u) (b) Q_4^{DD} (919/B_u)

Figure 3.23: The strongest coupled normal modes displacement vectors entering the 4-dimensional model for the HH and DD cases. These modes correspond to modes number 50 and 51, respectively, which are not shown in Tables 3.5 to 3.8 because they have almost zero two modes' couplings. In paranthesis the harmonic wave numbers (HH/DD in cm^{-1}) and the symmetries of the modes are given.

3.12 (mode number 7 is the low frequency mode).

Next, three more modes, Q_3^{HD}, Q_4^{HD} and Q_5^{HD}, had to be added after inspection of the third-order anharmonic force constants (see table 3.13) leading to 6D model for the HD case. The strongest coupled normal mode displacement vectors are shown in Fig. 3.24. The potential energy surface is analogous to that of Eq. 3.6.

As can be seen from Fig. 3.24 these modes involve skeleton rearrangements

No.	$\widetilde{\omega}$ (cm^{-1})	Q^0 (a$_o$(a.m.u)$^{1/2}$)	No.	$\widetilde{\omega}$ (cm^{-1})	Q^0 (a$_o$(a.m.u)$^{1/2}$)
7	195	6.10	44	879	-0.34
16	370	0.31	50	932	0.27
20	489	0.32	55	979	0.37
23	610	0.36	56	991	0.31
28	663	0.36	59	1033	0.23
29	673	-0.30	70	1274	-0.21
40	830	0.52	95	2550	0.61

Table 3.11: The normal modes coupled to the displaced mode Q_1^{HD} (ΔQ_1^{HD} = 0.03 a$_o$(a.m.u)$^{1/2}$), their wave numbers and their displacement from the equilibrium position.

No.	$\widetilde{\omega}$ (cm^{-1})	Q^0 (a$_o$(a.m.u)$^{1/2}$)	No.	$\widetilde{\omega}$ (cm^{-1})	Q^0 (a$_o$(a.m.u)$^{1/2}$)
7	186	9.75	55	976	0.57
19	470	-0.33	56	987	0.52
20	489	0.45	57	1011	0.23
23	609	0.54	64	1136	-0.22
28	663	0.24	70	1279	-0.33
29	673	-0.52	73	1319	-0.35
40	829	0.66	87	1538	0.25
42	833	0.39	94	1659	0.23
44	876	-0.53	95	2552	0.59
51	949	0.26	96	2365	-1.12

Table 3.12: The normal modes coupled to the displaced mode Q_2^{HD} (ΔQ_2^{HD} = 0.03 a$_o$(a.m.u)$^{1/2}$), their wave numbers and their displacement from the equilibrium position.

as well as substantial NH (Q_3^{HD}, Q_4^{HD}) and ND (Q_5^{HD}) bending. The coupling constants exceeding 30 $h{\cdot}c{\cdot}cm^{-1}$ are of two-mode origin, i.e., K_{113} = -127.38 $h{\cdot}c{\cdot}cm^{-1}$, K_{223} = 75.53 $h{\cdot}c{\cdot}cm^{-1}$, K_{224} = 140.45 $h{\cdot}c{\cdot}cm^{-1}$ and K_{225} = -138.64 $h{\cdot}c{\cdot}cm^{-1}$. The largest three-mode coupling is K_{136} = -23.30 $h{\cdot}c{\cdot}cm^{-1}$, see Table 3.13.

Exemplary two dimensional cuts of the three multidimensional potential energy surfaces are shown in Fig. 3.25. These cuts reflect the symmetry with respect

HD			
ijk	K_{ijk} ($h{\cdot}c{\cdot}cm^{-1}$)	ijk	K_{ijk} ($h{\cdot}c{\cdot}cm^{-1}$)
333	-4.44	455	1.32
444	3.71	664	-0.01
555	-1.81	665	-3.69
113	-127.38	114	15.43
223	75.53	115	-10.05
663	2.73	224	140.45
344	8.21	225	-138.64
355	5.26	655	2.38
133	-2.30	123	1.29
233	1.54	163	-23.30
633	0.84	164	8.55
334	1.95	145	-3.07
335	12.85	125	5.98
144	5.78	165	0.31
244	-3.00	263	-17.90
644	4.53	264	-17.77
445	20.85	265	7.70
255	-28.97	365	9.65

Table 3.13: The third-order force constant values which contribute in the anharmonic potential energy surface for HD case of porphycene. It was obtained from a combined calculations of the analytical second order force constants and finite differences.

to $Q_2^{HH/DD}$ = 0 for the cases HH and DD. This symmetry does not exist in the HD case due to the asymmetry resulting from different masses of hydrogen and deuterium. Figure 3.25 reveals the anharmonic mode coupling that results in a distortion of the potential energy surfaces, compared to the harmonic case. The potential energy surfaces in the negative directions of $Q_1^{HH/HD/DD}$ coordinate are steeper than for the positive directions because the displacement of this mode in the negative direction brings the hydrogen and nitrogen atoms closer which results in the steepness of the potential surface. For the same reason the potential is steep in the negative direction of Q_2^{HD}. Since the normal modes have been chosen, the minima of the potential energy surfaces will remain at **Q** = 0 which correspond to

the equilibrium distances in the classical nuclei limit. The largest distortion in the potential energy surfaces was observed in the cuts relating the symmetric stretch with the mode describing the N-N distance ($Q_3^{HH/DD}$ or Q_6^{HD}). Therefore, these two modes are strongly coupled which emphasizes what has been discussed in the introduction section, see Fig. 1.11, and shown experimentally by Gil [167] for the case of HH.

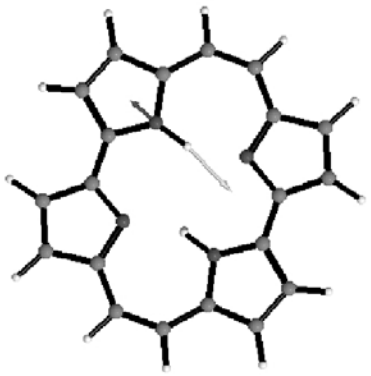

(a) Q_1^{HD} (2892)

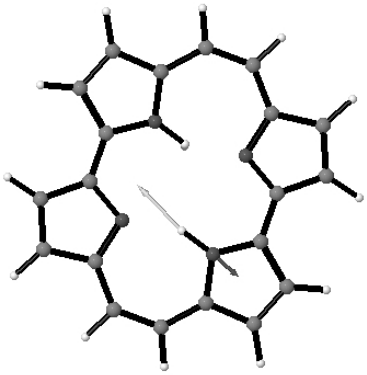

(b) Q_2^{HD} (2155)

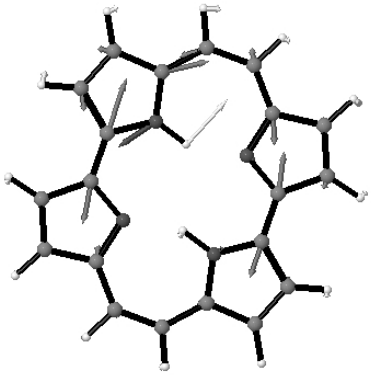

(c) Q_3^{HD} (1652)

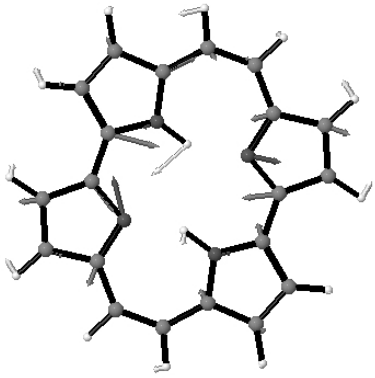

(d) Q_4^{HD} (1322)

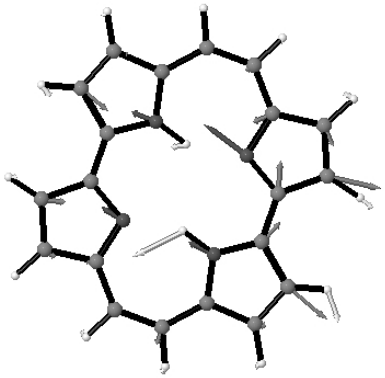

(e) Q_5^{HD} (929)

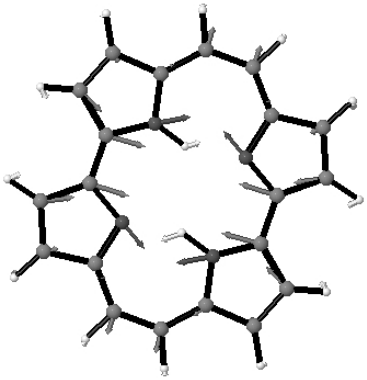

(f) Q_6^{HD} (186)

Figure 3.24: The normal mode displacement vectors corresponding to the (a) N-H and (b) N-D stretching vibrations for the HD case. The strongest coupled normal mode displacement vectors for the 6-dimensional model potential energy surface in the HD case (c) - (f). The harmonic wave numbers are given in paranthesis (in cm^{-1}).

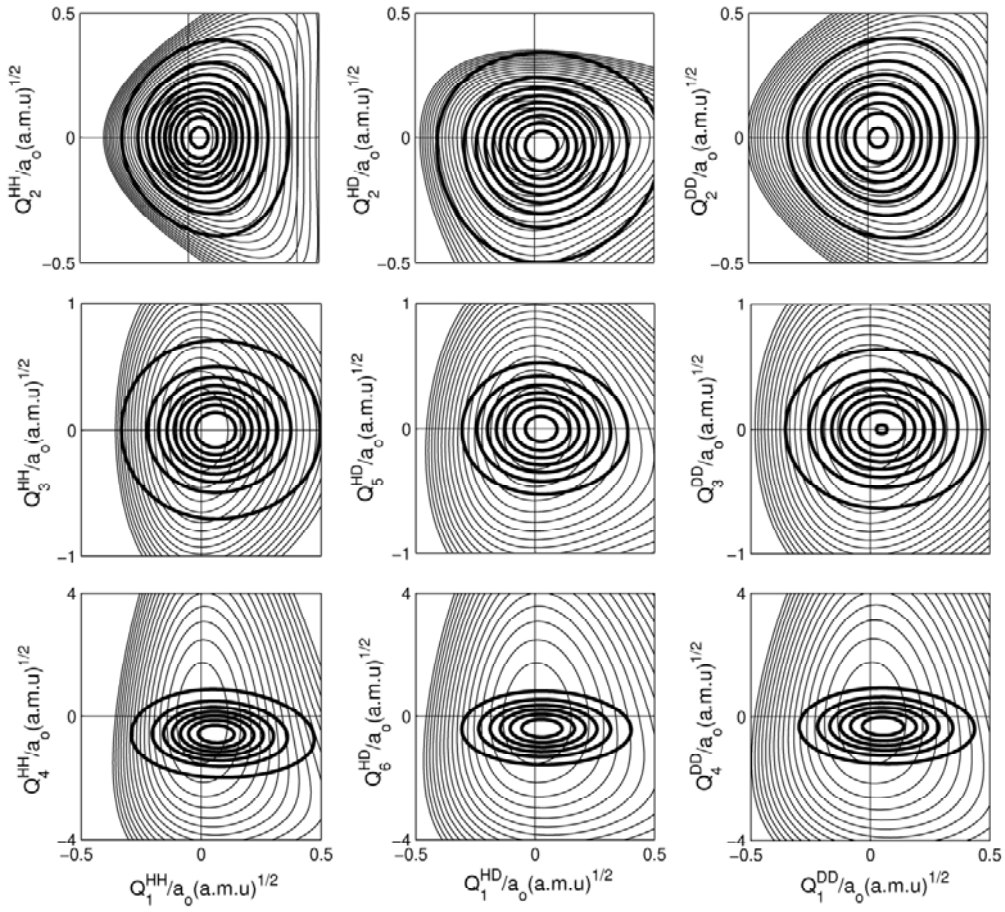

Figure 3.25: Exemplary two dimensional cuts of the multidimensional potential energy surfaces of porphycene (HH, HD, DD) together with the respective ground state vibrational probability distribution functions. The contour spacing for the potential (in eV): 0.05 to 1.00 in steps of 0.05 (first row), 0.05 to 0.80 in steps of 0.05 (second and third rows).

3.4 Ground-state nuclear wave functions and geometric H/D isotope effect

The effect of the mode-mode couplings on the wave functions will be discussed. The quantum correction of the employed normal mode coordinates on the anharmonic potential energy surface and its effect on geometries of the different isotopomers of porphycene will be explored, see section 1.1.3. This correlation will be translated into the so called geometric H/D isotope effects. Having defined the Hamiltonian, eqn. (3.2), the ground-state wavefunctions were calculated using the multiconfiguration time-dependent Hartree approach [132] together with imaginary time relaxation technique [164]. The calculations have been performed using the Heidelberg MCTDH program package [148]. For the harmonic oscillators, the discrete variable representation has been used on the grids (in $a_0(a.m.u.)^{1/2}$): $Q_{1/2}^{HH/HD/DD}$ [-0.65:0.65] (64 points), $Q_3^{HH/DD}$ [-6.5:6.5] (128 points), Q_3^{HD} [-1.5:1.5] (64 points), $Q_4^{HH/HD/DD}$ [-1.5:1.5] (64 points), Q_5^{HD} [-1.5:1.5] (64 points) and Q_6^{HD} [-6.5:6.5] (128 points), see Fig. 3.24. Moreover, we used four single particle functions for the combined modes ($Q_1^{HH/DD}$/$Q_2^{HH/DD}$; $Q_3^{HH/DD}$/$Q_4^{HH/DD}$) to capture strong mode-mode couplings, see Eq. (2.120) (the inputs are given in Appendix C). The resulting vibrational ground state probability distributions are shown in Fig. 3.25. Mere visual inspection of Fig. 3.25 reveals that the maxima of these distributions do not coincide with the configuration of the potential energy surfaces minima, that is, they are shifted according to the distortion of the potential energy surfaces. For instance, the coupling $V^{(2)}(Q_1^{HH/DD}, Q_{2/4}^{HH/DD})$ shifts the maximum of the probability density in case of HH and DD to positive $Q_1^{HH/DD}$, whereas $V^{(2)}(Q_1^{HH/DD}, Q_3^{HH/DD})$ causes a shift along positive $Q_1^{HH/DD}$ and $Q_3^{HH/DD}$, this is on one hand. On the other hand, HD case reflects shifts for all coordinates, i.e. the maximum of the probability density is shifted to positive Q_1^{HD} and $Q_{2/5/6}^{HD}$ mainly due to the coupling $V^{(2)}(Q_1^{HD}, Q_{2/5/6}^{HD})$. In order to quantify this deviation we have calculated the expectation values of the model coordinates (in units of $a_0(a.m.u.)^{1/2}$). For the HH case we obtain: $\langle Q_1^{HH} \rangle$ = +0.07, $\langle Q_2^{HH} \rangle$ = $\langle Q_4^{HH} \rangle$ = 0.00 and $\langle Q_3^{HH} \rangle$ = -0.48, whereas for the DD case we have $\langle Q_1^{DD} \rangle$ = +0.05, $\langle Q_2^{DD} \rangle$ = $\langle Q_4^{DD} \rangle$ = 0.00 and $\langle Q_3^{DD} \rangle$ = -0.26. For the asymmetric HD case, the expectation values of all coordinates differ from zero; $\langle Q_1^{HD} \rangle$ = +0.04, $\langle Q_2^{HD} \rangle$ = -0.05, $\langle Q_3^{HD} \rangle$ = -0.01, $\langle Q_4^{HD} \rangle$ = +0.02, $\langle Q_5^{HD} \rangle$ = -0.01 and $\langle Q_6^{HD} \rangle$ = -0.34. The different expectation values are clear indication of the geometric isotope effects. Notice that these values reflects

the combined effect of anharmonicity and quantum mechanical zero point energy.

In order to translate these expectation values into a geometric change, as explained in section 1.1.3, to probe the geometric H/D isotope effect, one can displace the equilibrium geometry along the normal mode coordinates according to these expectation values. From the obtained geometry we have calculated the corresponding new hydrogen bond parameters R_{NH}, R_{NN} and $R_{N...H}$ which contain the quantum correction on the anharmonic potential energy surface.

Table 3.14 summarizes the hydrogen bond parameters, R_{NH}, R_{NN} and $R_{N...H}$ as well as the NHN angle for the HH, HD and DD cases. Notice that the anharmonicity of the potential energy surfaces combined with the quantum nature of the nuclei causes an NH bond elongation of 0.031 Å for the HH case as compared to the classical approximation. As a consequence the hydrogen bond contracts, that is, R_{NN} shortens by 0.027 Å and $R_{N...H}$ by 0.056 Å. In other words, measured by the two NN distances the hydrogen bond becomes stronger when taking nuclear quantum effects (the zero-point energy in the anharmonic potential energy surface) into account. Upon double deuteration the hydrogen bond is weakened. Compared to the HH case the ND distance is shortened by 0.014 Å (primary geometric H/D isotope effect) while R_{NN} (secondary geometric H/D isotope effect) and $R_{N...H}$ increases by 0.014 and 0.027 Å, respectively. Thus we found the order $R_{NH}^{class} < R_{NH}^{quant}(DD) < R_{NH}^{quant}(HH)$ (primary geometric H/D isotope effect), $R_{N...H}^{class} > R_{N...H}^{quant}(DD) > R_{N...H}^{quant}(HH)$ and $R_{NN}^{class} > R_{NN}^{quant}(DD) > R_{NN}^{quant}(HH)$ (secondary geometric H/D isotope effect). This reflects the multidimensionality of the hydrogen bond which in the present case leads to a bond that is stronger in the quantum case as compared to the classical one. Double deuteration causes the quantum effects to diminish, that is, the hydrogen bond becomes weaker. In essence this is what is behind the so-called Ubbelohde or secondary geometric H/D isotope effect.

Focusing on the case of single deuteration (HD) we observe that the distance R_{NH} changes pretty much like in the HH and DD cases upon including quantum effects. Yet the quantum effect gets smaller in case of deuterated hydrogen bond relative to the non-deuterated one as expected. Moreover, this effect is moderate compared to the HH and DD cases. On the other hand, the distances R_{NN} take values which are about the same for both hydrogen bonds and which are intermediate between the HH and DD cases. In other words, single substitution leads to a weakening of both hydrogen bonds (what we call vicinal effect) as compared to the HH quantum case. This effect on the R_{NN} reveals that the cavity hosting the

hydrogen bonds is keeping the molecular symmetry.

	Classical	HH(4D)	HD(6D)		DD(4D)
			H	D	
$r_1 = R_{NH}$	1.049	1.080	1.078	1.067	1.066
$r_2 = R_{N...H}$	1.678	1.622	1.630	1642	1.649
R_{NN}	2.655	2.628	2.636	2.637	2.642
$\angle$ NHN	152.8	152.6	152.8	152.8	152.7

Table 3.14: The hydrogen bond parameters (in Å and degrees) as calculated by the conventional method (classical nuclei) and from the coordinates expectation value for four- and six-dimensional potential energy surface for HH/DD and HD, respectively.

It should be emphasized that the choice of the selected normal mode coordinates, of course, limits possible deformation of the structure. Nevertheless, these stretching modes have been chosen since the antisymmetric and symmetric NH stretching modes clearly should have a large projection on the reaction path, which in principle could be either concerted or stepwise, as shown in Cartesian reaction surface and Cartesian reaction plane Hamiltonian. If one settles with these two modes, the choice of the other modes is dictated by the anharmonicity of the potential energy surface. Thus the present four- and six-dimensional models should provide enough flexibility to describe the displacement of the two hydrogen bonds in porphycene in the vicinity of the trans isomer minimum.

3.5 Comparison between theoretical and NMR experimental results

A correlation between the NMR chemical shifts and geometric H/D isotope effects will be reported. Moreover, another correlation between the two hydrogen bond coordinates q_1 and q_2 will be presented. The relation between these correlation and the mechanism of the proton transfer will be discussed. The theoretically calculated geometric H/D isotope effect and NMR experimental results of Limbach and coworkers [170] will be compared.

In order to compare our theoretical results with experimental ones, we use NMR as the experimental reference for the determination of the geometric H/D

isotope effect. As mentioned in section 1.1.3, a direct measurement of the geometric H/D isotope effects using X-ray diffraction is not precise enough to analyze tiny changes in hydrogen bond geometries upon deuteration. Moreover, semideuterated samples would give only averaged distances over both N...H-N and N-D...N hydrogen bonds, what is insufficient for our study. This is why the NMR results are used for comparison with the quantum geometric H/D isotope effects.

In this context, the ^{1}H and ^{2}H NMR spectra of partially deuterated porphycene and its derivatives were recorded by Limbach and coworkers [170], and the chemical shifts of different isotopomers, $\delta_{\underline{H}H}$, $\delta_{\underline{H}D}$, $\delta_{\underline{D}H}$ and $\delta_{\underline{D}D}$ were measured. Using Eq. (B.7), the valence bond order model [171, 172, 173, 28], experimental geometries of porphycene and porphyrin [151] and adapting an experimental model published recently for the N-H..O hydrogen bond [43] to the N-H...N case (for more details see Ref. [170]), one can establish a correlation between proton/deuteron chemical shifts and geometric parameters q_1 and q_2, For details see Refs. [22, 174, 42, 43, 175, 176]. Therefore, one can predict the primary and secondary H/D geometric isotope effects.

From Table 3.14 we recognize that the NHN angle is not much influenced by quantum effects and deuteration, i.e., we can assume that $r_1 \approx \mathrm{R}_{NH}$ and $r_2 \approx \mathrm{R}_{N...H}$. Therefore, q_1 can be considered as the deviation from the hydrogen bond center and q_2 is the distance between the heavy atoms involved in the hydrogen bond, as depicted in Fig. 1.8. The q_1 and q_2 values obtained from the analysis of experimental data can be collected and drawn in the so called correlation curve, see Fig. 3.26.

Figure 3.26 depicts that the q_1 value switches sign on going from one isomer to the other. As q_1 decreases (the proton approaches the center of the hydrogen bond), q_2 decreases till a minimum value at the transition state and increases again when q_1 switches sign. The q_1 and q_2 values of porphycene are collected in Table 3.15 (for more details see Ref. [170]).

In order to compare our theoretically calculated geometries with experimental ones, we converted r_1 and r_2 from Table 3.14 to q_1 and q_2. As mentioned in section 3.1, the keypoint for the study of the tautomerization mechanism is the single deuteration case. Upon deuteration of porphycene to a certain extent (for instance, with a deuteron fraction X_D = 0.25), one has a normal, single and double deuterated species which upon ^{1}H NMR measurement gives two broad peaks, one for normal species (HH) and the other for single deuteration species (HD), see

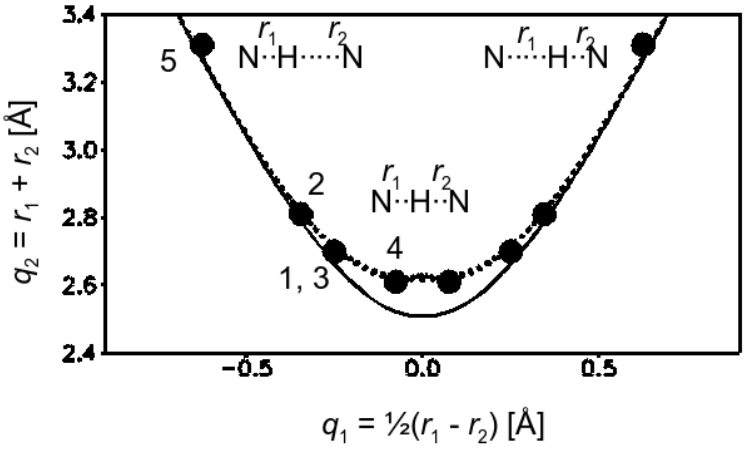

Figure 3.26: Correlation of the hydrogen bond length q_2 with the proton transfer coordinate for porphycene (1), 2,3,6,7,12,13,16,17-octaethylporphycene (2), 2,7,12,17-tetra-n-porphycene (3) (coinciding with (1)), 2,7,12,17-tetra-(tert-butyl)-3,6,13,16-dibenzo[cde;mno]porphycene (4) and porphyrin (5). The calculated solid curve represents equilibrium geometries, the dotted curve includes an empirical correction for anharmonic ground state vibrations [42]. This figure is adapted from Ref. [170].

	HH	HD		DD
		H	D	
q_1	0.2500	0.2559	0.2656	0.2706
	(0.2700)	(0.2750)	(0.2870)	(0.2905)
q_2	2.7000	2.7059	2.7147	2.7200
	(2.7020)	(2.7080)	(2.7090)	(2.7150)

Table 3.15: The hydrogen bond length q_2 = (r_1 + r_2) and the hydrogen-transfer coordinate q_1 = (r_1 - r_2)/2 obtained from NMR experimental results. In paranthesis the theoretical values according to Table 3.14 are given.

the upper panel of Fig. 3.27. Moreover, ^{2}H NMR measurement (for the same deuteron X_D = 0.25) gives two broader peaks, one for the single deuteration (DH) and the other of the double deuteration (DD), see the lower panel of Fig. 3.27.

Comparing experiment and theory in Fig. 3.28 we should take into account the following points: (i) There are several sources of experimental errors arising from the deconvolution of the chemical shift data, their correlation to q_1 values as well as the $q_1 - q_2$ correlation. (ii) The level of quantum chemistry as well as the

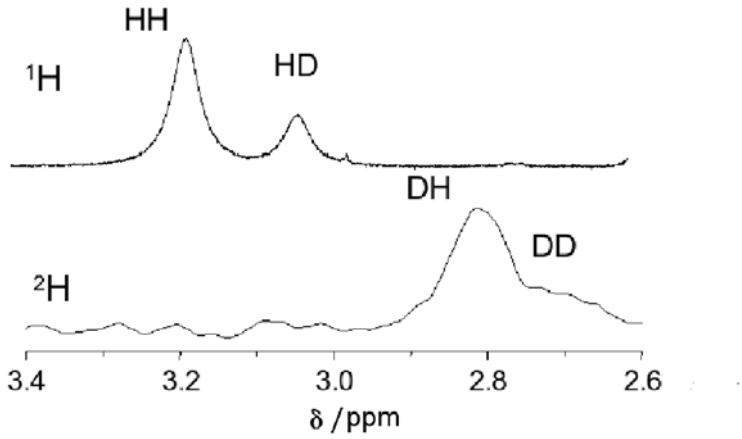

Figure 3.27: Inner proton (upper) and deuteron (lower) NMR signals of partially deuterated porphycene dissolved in CD_2Cl_2. The deuteron fraction X_D = 0.25. This figure is adapted from Ref. [170].

reduced dimensionality model are introducing an error which will be similar for all isotopomers, although difficult to quantify. Consider the primary geometric H/D isotope effect, that is, the change of q_1 which is shown in the upper panel of Fig. 3.28. Here, the agreement between theory and experiment is excellent as far as the relative change is concerned. The absolute theoretical values are almost uniformly too large by 0.02 Å. For the secondary geometric H/D isotope effect, that is, the change of q_2 between HH and DD is underestimated. For the HD case, theory predicts a rather concerted expansion of both hydrogen bonds. The experimental data indicate a similar cooperativity although the expansion is not as symmetric. Given the expected error limits discussed above the overall agreement between experiment and theory is satisfactory, thus substantiating the conclusion that the two intramolecular HBs in porphycene are behaving cooperatively. Returning to our working hypothesis, our findings for porphycene do not yet support the conclusion that the cooperativeness expressed in the geometrical changes also leads to a preference for concerted double hydrogen transfer. In order to address this point and to establish a firm relation between the quantum effects on the geometry and the kinetics as well as the dynamics of hydrogen bonds further studies will be necessary like the kinetic H/D isotope effect.

3.6 Kinetic H/D isotope effect

In this section the mechanism, concerted or stepwise, of tautomerization of porphycene will be explored, using as a tool the distinct way in which the rates of each of these mechanisms is influenced by deuteration. This is a collaboration work with our Canadian partner, Z. Smedarchina, who evaluated the rates of tautomerization which include the tunneling rate (from instanton approach) and the over-the-barrier rate (from the transition state theory). The evaluation of the tautomerization rates is based on our quantum chemical calculations of the stationary points and harmonic frequencies of porphycene (see section 3.1). These tautomerization rates are evaluated using some fitting parameters (calculated from fitting the theoretical rates to the experimental rates from Limbach [151]).

3.6.1 Tautomerization mechanisms and potential energy surface

In order to understand the dynamics of a chemical system, like the tautomerization mechanism, one needs to understand all the forces operating within the system, i.e. calculation of the potential energy surfaces is required. The dynamics of double-proton transfer reactions in porphycene can be investigated by performing ab initio calculations of the potential energy surface and the transfer rates can be calculated afterwards. As mentioned in section 1.1.3, the shape of the potential energy surface may reflect the mechanism of the double proton transfer. The stationary points on the potential energy surface have been calculated by means of density functional theory (B3LYP/6-31+G(d,p)), as implemented in Gaussian03 program package [155], see section 3.1. This potential energy surface is similar to that predicted for porphyrin [52]. This type of potential energy surface suggests two tautomerization mechanisms that are the stepwise mechanism, via the cis intermediate and the corresponding transition state, and the concerted mechanism, via the transition state connecting the two trans tautomers, whereby the symmetric N-H stretch is the reaction coordinate.

In general, different pathways corresponding to double proton transfer may be coupled and the evaluation of the rate constant of tautomerization becomes a complex task. As proposed in Ref. [177], the two pathways are considered as uncoupled, i.e. if the symmetric stretching vibrations is considered as the reaction coordinates for the concerted pathways, one can keep the antisymmetric stretching vibration frozen. The rate constants of tautomerization for the concerted as

well as for the stepwise mechanisms, were evaluated by Z. Smedarchina using the AIM/DOIT program [178]. Calculations of the rate of the concerted mechanism follow the scheme for the carboxylic acid dimers [179]. The calculations of the rates of the stepwise mechanism follow the scheme applied for porphine [52]. The rate constant for the stepwise mechanism is evaluated as the rate of a two-step process through the intermediate and the transition state. In the case of stepwise transfer of the combination AB (A,B = H or D), the corresponding rate constant is given by the general expression (see Appendix A):

$$k_{SM}^{AB} = M\big(\frac{k_1^A k_2^B}{k_{-1}^A + k_2^B} + \frac{k_1^B k_2^A}{k_{-1}^B + k_2^A}\big), \tag{3.7}$$

where k_1^A, k_1^B are the rate constants of trans-cis transition of the particles A and B, respectively, and M = 2 is the number of channels. Due to the symmetry of porphycene the rates for HH and DD transfer reduce to

$$k_{SM}^{HH} = Mk_1^H \qquad \& \qquad k_{SM}^{DD} = Mk_1^D. \tag{3.8}$$

The rate constant for the combination of mixed isotopes HD is then given by

$$k_{SM}^{HD} = M\big(\frac{k_1^H k_2^D + k_1^D k_2^H}{2(k_2^H + k_2^D)}\big). \tag{3.9}$$

As discussed in section 1.1.4, tunneling can be accounted for by instanton techniques, whereby the rate constant is proportional to $exp(-S(T))$ [54, 52], where one does not need an explicit knowledge about the instanton trajectory but rather the instanton action. The total rate is then a sum of a tunneling (k_{AIM}) and classical components (k_{TST}):

$$k(T) = k_{AIM}(T) + k_{TST}(T), \tag{3.10}$$

which reflect the through- and over-barrier pathways. The components k_{AIM} and k_{TST} in the AIM/DOIT approach are evaluated by the AIM and TST, respectively [180].

The free-energies at T=298 K, obtained from the energies and force fields of the stationary configurations (B3LYP/6-31+G(d,p)), are characterized by the following (relative) values: $G_{trans} = 0$, $G_{TS} = 1.07$ kcal/mol, $G_{cis} = 1.76$ kcal/mol, i.e. the cis configuration becomes a maximum (see also discussion in Section 3.1 and Fig. 3.6). Therefore, the two step process turns into a single step with a barrier of 1.76 kcal/mol, i.e. the stepwise mechanism is not supported by such a potential energy surface. This value is very small as compared to the experimental value of the activation energy which is 6 kcal/mol [151]. Nevertheless, the

cis-trans barrier of the effective potential including the effect of mode-coupling governing the proton transfer [52, 177] is calculated to be 6 kcal/mol indicating clearly that a stepwise mechanism is possible. Accordingly, the rate constant has been calculated by Z. Smedarchina according to Eq. (3.10) for the stepwise as well as the concerted mechanisms. The calculated rate constants are collected in Table 3.16. The experimental data of the rate constants in the temperature range 228-335 K (Fig. 3.29) show a value of $5 \cdot 10^7$ s^{-1} at 300 K which is in poor agreement with the calculated rate constants. Moreover the experimental value of the activation energy is also higher than that of the calculated values. Therefore the actual barrier height will substantially exceed the observed activation energy. Hence one may conclude that the calculated barriers can be incorrect.

Parameter	**Concerted mechanism**	**Stepwise mechanism**
$k(300)$, s^{-1}	2×10^9	3×10^{10}
E_a, kcal/mol	4.3	3.0

Table 3.16: The rate constants of the concerted as well as the stepwise mechanisms for porphycene calculated by Z. Smedarchina at the B3LYP/6-31+G(d,p) level [177].

In order to reproduce the experimental rate constants, another strategy is adopted that is the geometries and force fields of the calculated potential energy surface (B3LYP) are used but the barrier height is fitted. Recalling energetics (in kcal/mol) of the stationary points of porphycene using B3LYP/6-31+G(d,p), we get the values given in Table 3.17.

	B3LYP/6-31+G(d,p)	scaled
E(trans)	0.0	0.0
E(cis)	2.3	4.5
$E_{TS(cis,trans)}$	4.7	10.9
$E_{TS(trans,trans)}$	6.5	$>$10.0

Table 3.17: Energetics (in kcal/mol), without zero point correction, of the stationary points of porphycene using B3LYP/6-31+G(d,p) level of theory and the scaled values obtained by fitting the calculated rates with the experimental values by Limbach, see Fig. 3.29.

This fitting corresponds to E(cis)=4.5 kcal/mol rather than 2.3 kcal/mol and $E_{TS(cis,trans)}$ = 10.9 kcal/mol rather than 4.7 kcal/mol. In addition $E_{TS(trans,trans)}$ needs to be increased to a value of more than 10 kcal/mol. Although the fitting obtained with these values, illustrated in Fig. 3.29, is satisfactory, it seems unlikely that the calculated potential energy surface will be in error by these large amounts. Therefore, an interpretation of the tautomerization dynamics in terms of stepwise transfer must be ruled out.

The calculated rate constants for concerted mechanism are much closer to the experimental values than those for stepwise mechanism. Assuming that there is no stable cis configuration, and adjust $E_{TS(trans,trans)}$ from 6.4 to 6.8 kcal/mol, the approximate fit to the kinetic data displayed in Fig. 3.30 is obtained. Overall, the fit is as good as that of Fig. 3.29 but requires much less drastic adjustment of the calculated potential energy surface. Further, Fig. 3.30 displays calculated HD and DD rate constants (concerted pathway) for the adjusted potentials and thus present estimates of the kinetic H/D isotope effect. The concertedness of the transfer should support our "*working hypothesis*", that is, "*cooperativity*" can be used to reveal the mechanism (cf. section 3.3). However, experimental studies of HD and DD kinetic isotope effect are required to give further support for the conclusion.

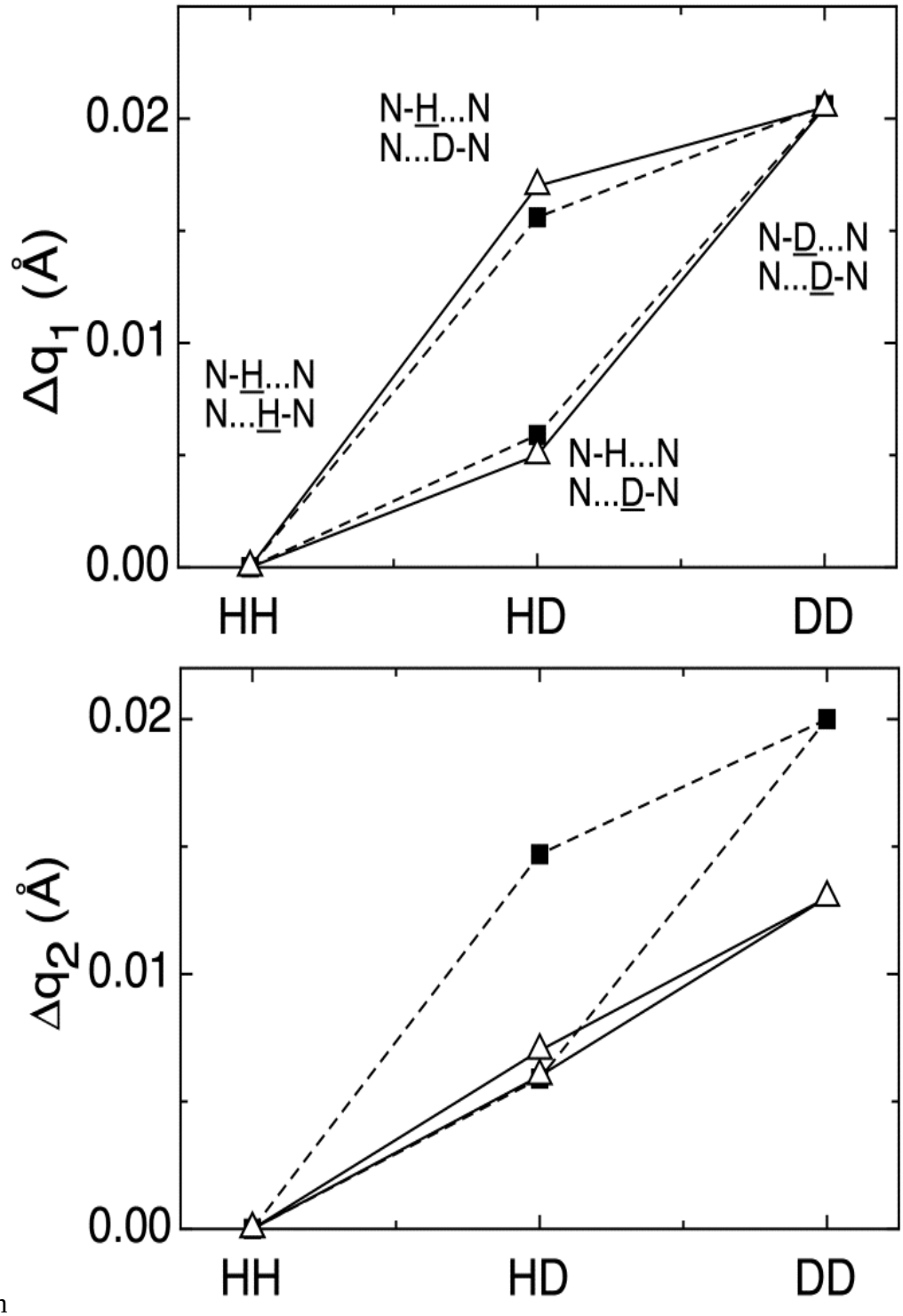

cm

Figure 3.28: Comparison of theoretical (open triangles) and experimental (solid boxes, adapted from Ref. [170]) values of the change of the hydrogen bond parameters q_1, primary geometric H/D isotope effect, (upper panel) and q_2, secondary geometric H/D isotope effect, (lower panel) with respect to the HH case of porphycene HH,HD,DD.

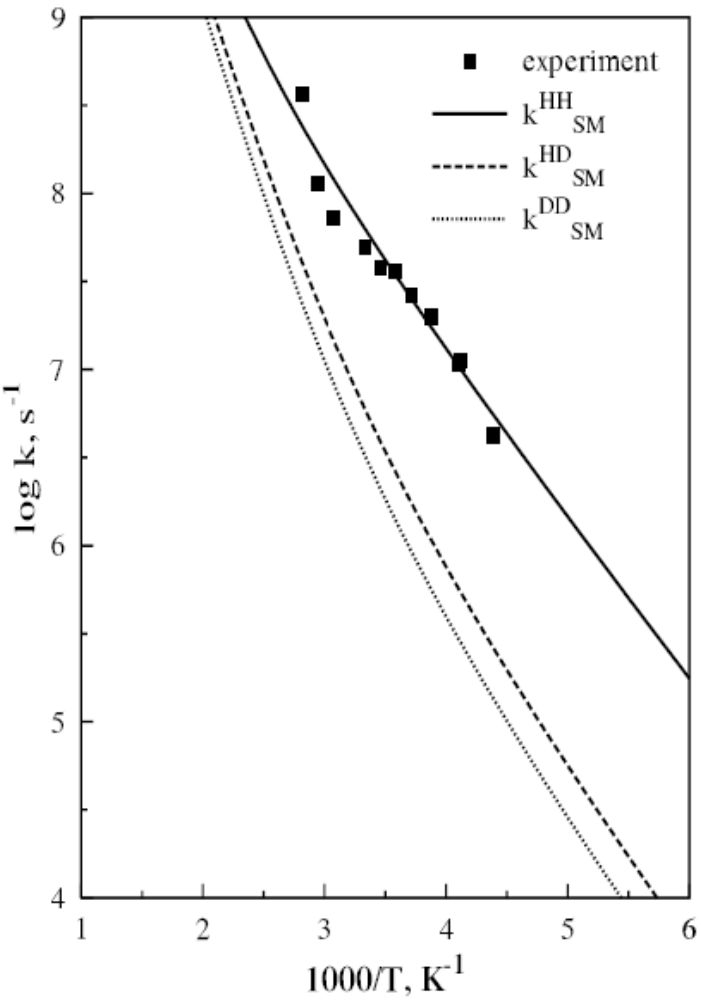

Figure 3.29: Rate constants for the stepwise mechanism obtained by the AIM/DOIT approach for the potential energy surface at the B3LYP/6-31+G(d,p) level with E(cis), $E_{TS(cis,trans)}$ and $E_{TS(trans,trans)}$ adjusted to yield the best fit to the points representing the experimental data of Limbach [151]. The calculated curves represent stepwise transfer for HH, HD and DD.

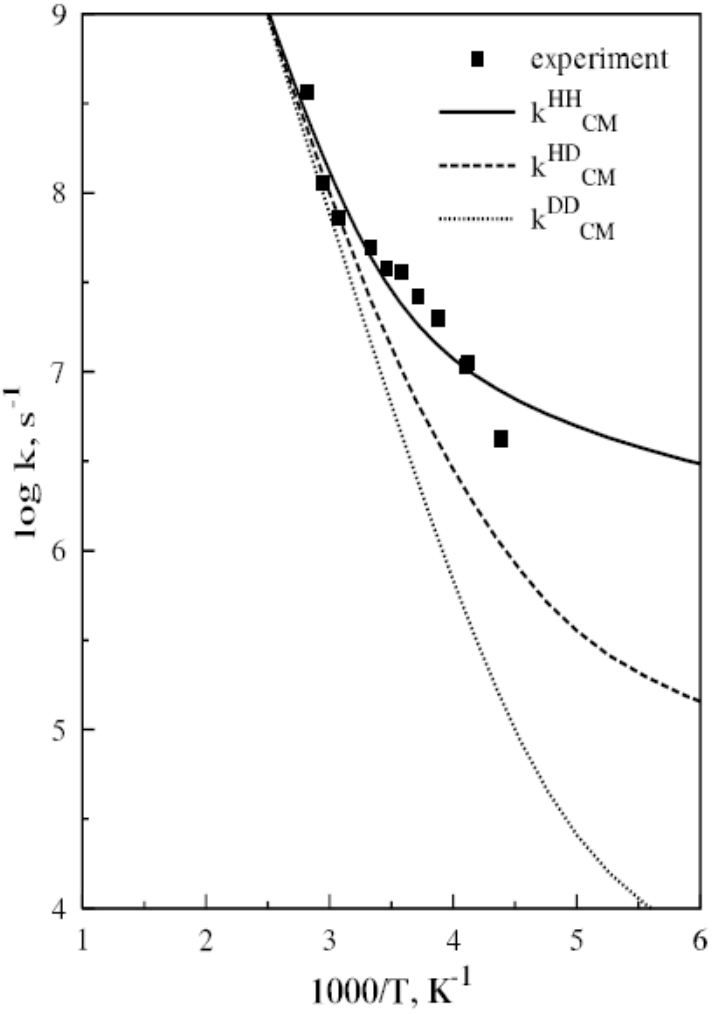

Figure 3.30: Same as in Fig. 3.29, for the potential energy surface with alternative adjustments that render the cis configuration unstable. The calculated curves represent concerted transfer for HH, HD and DD.